

Department of Physics and Astronomy

University of Heidelberg

Master thesis

in Physics,

submitted by

Christian Sand,

born in St. Ingbert

– 2018 –

Hydrodynamics of an AGB star during the Common Envelope Phase

This Master thesis has been carried out by Christian Sand

at

Heidelberg Institute for Theoretical Studies

under the supervision of

Prof. Dr. Friedrich Röpke

Hydrodynamik eines AGB-Sterns während der Phase der Gemeinsamen Hülle:

Wir betrachten die Entwicklung eines Systems einer Gemeinsamen Hülle, bestehend aus einem Asymptotischen-Riesenast-Stern und einem Weißen Zwerg. Während der Phase der Gemeinsamen Hülle umschließt der Riesenstern seinen Begleiter, der Transfer von Drehimpuls und Energie führt zum Hineinspiralieren des Begleitsterns in die Hülle, die zumindest teilweise ausgestoßen und gravitativ vom System entbunden wird; es resultiert ein enges Binärsternsystem. Der Ausstoßmechanismus selbst ist immer noch nicht gut verstanden.

Nach dem Mappen eines eindimensionalen Sternenprofils von MESA auf das Gitter und dem Relaxieren der Atmosphäre des Riesen, um ein stabiles Modell zu erhalten, führen wir eine dreidimensionale Hydrodynamiksimulation mit AREPO auf einem bewegten, adaptiven Gitter durch. Hierbei können dynamische Instabilitäten beobachtet werden. Mithilfe verschiedener Begleitsternmassen diskutieren wir die Beiträge von Drehimpuls und verschiedener Energieformen zum Ausstoß der Hülle. Die Dynamik wird durch dynamische Reibung und Schocks bestimmt. Unter Berücksichtigung des Ionisationszustandes des Gases kann die Freisetzung von Rekombinationsenergie den ungebundenen Massenanteil deutlich erhöhen und die Hülle vollständig ausstoßen.

Hydrodynamics of an AGB star during the Common Envelope Phase:

We consider the evolution of a common envelope system, consisting of an asymptotic giant branch star and a white dwarf. During the common-envelope event, the giant star engulfs its companion, the transfer of angular momentum and energy leads to the spiral-in of the companion into the envelope, which is at least partially ejected and gravitationally unbound from the system; a close binary system results. The ejection mechanism itself is still not well understood.

After mapping a one-dimensional stellar profiles from MESA onto the grid and relaxing the giant's atmosphere in order to obtain a stable model, we perform a three-dimensional simulation of the hydrodynamics with AREPO on a moving adaptive mesh, where dynamical instabilities can be observed. With the aid of different companion star masses, we discuss the contributions of angular momentum and different forms of energy to the ejection of the envelope. The dynamics are governed by dynamical friction and shocks. Considering the ionization state of the gas, the release of recombination energy can significantly increase the unbound mass fraction, ejecting the envelope completely.

Erklärung:

Ich versichere, dass ich diese Arbeit selbstständig verfasst habe und keine anderen als die angegebenen Quellen und Hilfsmittel benutzt habe.

Heidelberg, den 18.05.2018

.....

Contents

1	Introduction	1
2	Physical Foundations	3
2.1	Hydrodynamics	3
2.2	Energy transport	5
2.3	Thermodynamics	6
2.4	Timescales	8
2.5	Single star evolution	9
2.6	Binary systems	10
2.7	Common envelope phase	13
2.7.1	Angular momentum	15
2.7.2	Energetics	15
3	Numerical Methods	19
4	Initial Models	21
4.1	Stellar profile	21
4.2	Mapping	22
4.3	Relaxation	23
4.4	Resolving the atmosphere boundaries	24
4.4.1	Resolving pressure scale height	24
4.4.2	Resolving the softening length	25
4.5	1.2 M _⊙ model resolution study	26
4.6	Influence of the EOS	27
4.7	Results	28
4.8	Model parameters	29
5	Common envelope simulation with 1.2 M_⊙ primary	30
5.1	Setup	30
5.2	Reference run	31
5.3	Angular momentum	34
5.4	Energetic considerations	35
5.5	Different companions	41

6	Common envelope simulation with $2.5 M_{\odot}$ primary	45
7	Conclusion	48
	Nomenclature	50
I	Appendix	51
A	Constants	52
B	List of Figures and Tables	53
	B.1 List of Figures	53
	B.2 List of Tables	53
C	Bibliography	55

1 Introduction

Multiple star systems are very common in star clusters or galaxies. They consist of a small number of stars, gravitationally bound and orbiting each other, in most cases without any noticeable interaction on long timescales. A system formed by only two stars is called *binary system*. The brighter star is denoted *primary*, the other one *secondary* or *companion*. If their orbits are close and mass transfer is possible, they are called *close binaries*, otherwise they are *wide binaries*.

The common-envelope event, first described by Paczynski [1976], is a short phase in which two stars¹ orbit in a single, shared envelope. Stars involved may be a red giant (RG) or asymptotic giant branch (AGB) and a compact companion, such as a white dwarf (WD) or a main sequence (MS) star. When the atmosphere of a giant expands, mass can be transferred to the companion, leading to a further expansion of the giant evolving towards its thermodynamical equilibrium. The loss of angular momentum leads to the inspiral, further increasing mass transfer. The companion can no longer accrete the mass, the core of the giant and its companion star orbit one another inside the common envelope. The transfer of angular momentum and energy may lead to the ejection of the envelope and a close binary system is formed by the giant's core and the companion star, which is relatively unaffected in terms of evolution. With a decreased separation, the stars may even merge. Possible outcomes, ranging from close double white dwarfs, progenitors of Type Ia supernovae to merging neutron stars (one source of gravitational waves detected so far), have a compact remnant in common (a white dwarf, neutron star or black hole) – the core of a formerly much bigger star with initial radii greater than the orbital separation of the objects after the evolution, which can be explained by the mass loss during the common-envelope event. Podsiadlowski [2012] proposes a classification for simulations for the determination of the outcome.

The properties of many compact objects observed cannot be explained by single star evolution, which draws attention to the influence of secondary stars. Due to its short timescale compared to the lifetime of a star, a common-envelope event has not been observed yet, so our analysis mainly consists of theoretical considerations. However, it is widely accepted as a mechanism for the formation of close binary system, also explaining observed close binary systems [Izzard et al., 2012]. There exist previous simulations that one can compare, mainly in one dimension. Ivanova and Nandez [2016] for instance studied the evolution and possible outcomes. Passy et al. [2012] performed a three-dimensional simulation with a red giant of similar mass as our AGB star and different companion masses.

¹The probability for more stars to be involved in such an event indeed is extremely small due to the orders of magnitude difference in timescales.

Energetic considerations are crucial for unbinding the envelope. The orbital energy (gravitational energy between the two stellar objects) set free by decrease in orbit for sure plays a major role. Another important energy source during the common-envelope event, when ionized material of the envelope expands and cools, i.e. densities and temperature decrease, is recombination, releasing previously stored ionization energy as recombination energy. We want to include this effect in our simulation, since the dynamics may be influenced.

Previous three-dimensional studies by [Ohlmann \[2016\]](#), conducted with a $2 M_{\odot}$ RG star as primary have shown the dynamics of the common-envelope event, considering also recombination energy. However, stability problems were encountered when trying to set up an AGB star with its even more extended envelope, that is only weakly bound.

The aim is to set up a stable model of an AGB star and perform a three-dimensional simulation of the hydrodynamics with AREPO [[Springel, 2010](#)] on a moving adaptive mesh. With the aid of different companion star masses, a discussion on the contributions of angular momentum and different forms of energy to the ejection of the envelope will help to understand the dynamics. We will take into consideration the release of recombination energy for the ejection of the envelope.

2 Physical Foundations

We begin with giving an overview of all the physical mechanisms involved in the event of common envelope (CE). The flow of stellar matter can macroscopically be described by hydrodynamics with gravity (Section 2.1), its state and properties by thermodynamics (Section 2.3). Stellar evolution is described in Section 2.5, the binary system in presence of a companion in Section 2.6 and the special case of a common envelope event in Section 2.7.

2.1 Hydrodynamics

We use hydrodynamics in order to describe the flow of gases¹. It is based on conservation laws for mass, balance of energy (first law of thermodynamics) and linear (and angular) momentum (Newton’s second law of motion).

Fluids are composed of particles colliding with each other on scales (in this case one speaks of the *mean free path*) much smaller than the size of the system, such that microdynamics can be neglected. Hydrodynamics namely ignores discrete particles and assumes continuum, i.e. physical quantities are defined continuously at every point in space. Long-range interactions such as gravity have to be included explicitly. The following sections are based on [Kippenhahn and Weigert \[1990\]](#) and [Benacquista \[2013\]](#).

Equations

For a system that can be considered a continuum with flow velocities small compared to the speed of light, hydrodynamics is described by the *Navier–Stokes equations*. For typical scales in astrophysics, the viscous forces can be neglected compared to inertial forces. The Navier–Stokes equations then simplify to the *Euler equations*

$$\begin{aligned}\frac{\partial \rho}{\partial t} + \nabla(\rho \mathbf{v}) &= 0, \\ \frac{\partial \rho \mathbf{v}}{\partial t} + \nabla(\rho \mathbf{v} \otimes \mathbf{v} + p \mathbf{I}) &= \rho \mathbf{f}, \\ \frac{\partial \rho e_{tot}}{\partial t} + \nabla(\mathbf{v}(\rho e_{tot} + p)) &= \rho \mathbf{v} \mathbf{f},\end{aligned}$$

with density ρ , velocity \mathbf{v} , pressure p and total specific energy $e_{tot} = \epsilon_{int}/\rho + \mathbf{v}^2/2$, which is energy per unit mass, with the internal energy density ϵ_{int} and an external force \mathbf{f} .

¹For historical reasons, the term *hydrodynamics* is basically used as a synonym for *fluid mechanics*, since their dynamics underlie the same principles.

Gravity

The external force in our case is gravity. Any mass density ρ causes a gravitational acceleration $\mathbf{g} = \nabla\Phi$ due to its gravitational field Φ according to *Poisson's equation*

$$\Delta\Phi = 4\pi G\rho. \quad (2.1)$$

Solving this elliptic differential equation of second order, we use the Dirichlet boundary condition, specifying values the solution needs to take at the boundary. The solution writes as

$$\Phi(\mathbf{r}) = G \int d^3r' \frac{\rho(\mathbf{r}')}{|\mathbf{r} - \mathbf{r}'|}. \quad (2.2)$$

We choose the constant of integration to be zero such that the potential vanishes at infinity. For a point mass M due to symmetry this is dependent only on the distance r and reads

$$\Phi(r) = G \frac{M}{r}. \quad (2.3)$$

The gravitational energy is defined as the work done by bringing a mass m from infinity to distance r ,

$$E_{grav} = \int_{\infty}^r G \frac{mM}{r'^2} dr' = -G \frac{mM}{r}. \quad (2.4)$$

This is independent of the path due to the conservative character of the vector field since it is derived from a potential.

Hydrostatic equilibrium

For our theoretical considerations we further assume spherical symmetry, isolation from the rest of the universe and uniform initial composition.

In a cloud collapsing under the effect of gravitation, there is an acceleration due to pressure counteracting (cf. momentum equation, second Euler equation in Section 2.1). This leads to

$$\ddot{r} = -\frac{Gm}{r^2} - 4\pi r^2 \frac{\partial P}{\partial m} \quad (2.5)$$

for a spherical setup. One can find an equilibrium ($\ddot{r} = 0$) for

$$\frac{dP}{dm} + \frac{Gm}{4\pi r^4} = 0 \Rightarrow \frac{\partial p}{\partial r} + g\rho = 0. \quad (2.6)$$

This is the so-called *hydrostatic equilibrium*.

Virial Theorem

Multiplying Equation 2.6 with factor $4\pi r^3$ and integrating over dm in the interval $[0, M]$ (from the center to the surface) by partial integration,

$$\int_0^M 4\pi r^3 \frac{dP}{dm} dm = [4\pi r^3 P]_0^M - \int_0^M 12\pi r^2 \frac{\partial r}{\partial m} P dm, \quad (2.7)$$

the terms in the brackets vanish ($r = 0$ at the center and $P = 0$ at the surface). Substituting for a mass shell with $\partial m = 4\pi r^2 \rho \partial r$ on the right-hand side, one can find

$$\int_0^M \frac{GM}{r} dm = 3 \int_0^M \frac{P}{\rho} dm, \quad (2.8)$$

where the left-hand side of the equation is equal to minus the *total gravitational energy* E_g . This is the general form of the *Virial Theorem*.

2.2 Energy transport

Energy can be transported in the following ways.

Radiation

From inside the star, where nuclear reactions set free energy, radiation transport brings it to outer layers.

The *luminosity* L is defined as the energy passing outwards through the surface per unit time.

In case of recombination, radiation transports energy away from the place of recombination. This is important in order to understand in which degree this energy source can help to unbind the envelope.

Convection

Instabilities in the radial direction, i.e. perturbations in the hydrostatic equilibrium, occur for a packet of gas of higher temperature (lower density) than its surroundings. It will rise until this difference is balanced.

A stratification with

$$\left(\frac{\partial \rho}{\partial r} \right)_{\text{parcel}} < \left(\frac{\partial \rho}{\partial r} \right)_{\text{surroundings}} \quad (2.9)$$

is stable.

Otherwise, the buoyancy due to a temperature profile $\nabla = \frac{d \ln T}{d \ln P}$ lets the parcel rise, we assume slowly enough to be in pressure equilibrium with its surroundings, but fast enough not to be in temperature equilibrium, i.e. as an adiabatic process.

The *Schwarzschild criterion* states stability against convection if $\nabla < \nabla_{ad}$ (assuming chemically homogeneous layers), where ∇_{ad} denotes the *adiabatic temperature gradient*,

$$\nabla_{ad} = \left(\frac{\partial \ln T}{\partial \ln P} \right)_S. \quad (2.10)$$

Convection is very efficient, the temperature gradient in convective zones thus is very close to the adiabatic temperature gradient.

2.3 Thermodynamics

Thermodynamics describes the state of a macroscopic system by means of microscopic considerations and statistics. It is based on the four axiomatic laws of thermodynamics: thermal equilibrium is transitive, energy is conserved, entropy cannot decrease, entropy is minimal at absolute zero.

Composition

Stars are heated by nuclear fusion. Thus, composition changes with time, which certainly will have an impact on the stellar structure.

For each nuclear species i , the composition of the star in terms of mass fraction is defined as $X_i \equiv \frac{\rho_i}{\rho}$ with density of this species ρ_i and total density ρ in a certain region.

Usually when talking about compositions, X is the mass fraction of hydrogen, Y for helium and Z for all heavier atoms, called metals.

Equation of state

In addition to the mass, momentum, and energy conservation equations, a thermodynamic relation is required to express the pressure as a function of other thermodynamic variables, the so-called the *equation of state* (EOS).

The *ideal gas law* is a simple EOS assuming perfectly elastic collisions as the only interaction:

$$PV = Nk_B T = nRT \Leftrightarrow P = \frac{N}{V} kT = \frac{\rho}{m} kT, \quad (2.11)$$

where R denotes the ideal gas constant and k_B the Boltzmann constant. For the pressure to support the star, if e.g. the gas particles' mass increase (as for nuclear fusion), the product of density and temperature has to increase as well.

Fully ionized gas, as it is expected inside stars due to the temperature, interacts mainly via the Coulomb force for charged particles. For solar values, this interaction contributes less than 1 % to the energies. The ideal gas law thus is suitable for the theoretical considerations in this chapter and we will use it for simplification.

The astrophysical *OPAL EOS* considers a mixture of the elements hydrogen, helium, carbon, nitrogen, oxygen and neon, and it is based on an activity expansion of the grand canonical partition function [Rogers and Nayfonov, 2002]. It takes into account Coulomb interactions between electrons and nuclei as well as ionization effects.

Ionization

Not only can atoms get to excited states by gaining energy. By gaining or losing electrons, atoms can acquire a negative or positive charge and form ions.

The *ionization energy* is defined as the energy necessary to remove the most loosely bound electron,

$$X + \text{ionization energy} \rightarrow X^+ + e^-,$$

where X denotes the atom, X^+ the positively charged ion and e^- the unbound electron. By losing further electrons, the atom can get additional positive charge. The inverse process is called *recombination*, releasing *recombination energy*.

Some values are 13.6 eV for hydrogen and 24.6 eV (54.4 eV) for the first (second) helium ionization.

It is thermal collisions of the atoms that ionize the gas. The electrons unbound from the atoms form an electron cloud surrounding the ions and neutral atoms. This mixture is called *plasma*. It generates an electric field, in which the motion of the charged particles generates a magnetic field.

The thermal contribution is calculated relating the average kinetic energy of particles in a gas with the temperature of the gas. The ratio of the probability for an atom to be in the excited state $n + 1$ to state n with the energy difference of $\psi = \epsilon_{i+1} - \epsilon_i$ is given by

$$\frac{n_{i+1}}{n_i} = \frac{g_{i+1}}{g_i} e^{-\psi/kT}, \quad (2.12)$$

where n_i denotes the density of atoms in the i -th state of ionization (i electrons removed), g_i is the degeneracy (states with same energy but different quantum numbers) and k the Boltzmann constant.

The *Saha equation* describes the degree of ionization for a gas as

$$\frac{n_{i+1}n_e}{n_i} = \frac{2}{\lambda_{th}^3} \frac{g_{i+1}}{g_i} e^{-\psi/kT}, \quad (2.13)$$

where λ_{th} denotes the thermal de Broglie wavelength.

In regions of lower densities and temperatures, ionization breaks up, *recombination* takes place, releasing *recombination energy*.

Opacity

Opacity is a measure for the impermeability to radiation, *opaque* is the opposite of transparent. There are different processes leading to opacity, including reflection and scattering, however, in the context of ionization, absorption is the most important. The opacity χ is the inverse of the mean free path. The intensity I of an incoming beam with the initial intensity I_0 after traveling the distance x in a medium with opacity χ will be reduced according to

$$I(x) = I_0 e^{-\chi x}. \quad (2.14)$$

Its value will generally depend on the wavelength, $\chi = \chi(\lambda)$.

Pressure

The total pressure P is equal to the sum of the pressure due to the single species the gas consists of plus the radiation pressure, counteracting gravity and leading to a stable, almost stationary state in the stellar interior.

$$P = P_I + P_e + P_{rad} = P_{gas} + P_{rad}, \quad (2.15)$$

with the ion pressure P_I (caused by the ions of the individual species i , $P_I = \sum_i P_i$), the electron pressure P_e and the radiation pressure P_{rad} , defining β as $P_{gas} \equiv \beta P$ and $P_{rad} = (1 - \beta)P$.

2.4 Timescales

We define timescales in general as

$$\tau \equiv \frac{\Theta}{\dot{\Theta}} \quad (2.16)$$

for a physical quantity Θ that changes with time (derivative with respect to time $\dot{\Theta}$). Considering radius R , mass M and gravitational constant G , the escape velocity due to gravity $v_{esc} = \dot{R} = \sqrt{2GM/R}$, the **dynamical timescale** (or free-fall timescale) gives an estimate how long such a star would need to collapse, resulting in

$$\tau_{dyn} \sim \sqrt{\frac{R^3}{2GM}}. \quad (2.17)$$

For the average density $\bar{\rho} \sim M/R^3$ and referring to the solar values, one finds

$$\tau_{dyn} \sim \frac{1}{\sqrt{G\bar{\rho}}} \approx (1.6 \times 10^3 \text{ s}) \sqrt{\left(\frac{R}{R_\odot}\right)^3 \left(\frac{M_\odot}{M}\right)}. \quad (2.18)$$

This very short timescale of about 15 min for the Sun means that the star is either in an hydrostatic equilibrium shortly after perturbation or gets destroyed. The dynamical timescale can in principle also estimate the time for the propagation of an hydrodynamic disturbance within the star. A better choice for this however is the *acoustic timescale* (or sound-crossing time) τ_s . For a disturbance to propagate from the center of the star to radius r ,

$$\tau_s(r) = \int_0^R \frac{dr'}{c_s(r')}, \quad (2.19)$$

where c_s denotes the speed of sound. For giant star models, this timescale (up to the surface at $r = R$) is in the order of $\tau \sim 10^6$ s.

The **thermal timescale** (or Kelvin-Helmholtz timescale) estimates in what time a star with given radius and mass could radiate away its gravitational energy GM^2/R by luminosity L , thus

$$\tau_{th} \sim \frac{U}{L} \sim \frac{GM^2}{RL} \approx (3.1 \times 10^7 \text{ yr}) \left(\frac{M}{M_\odot} \right)^2 \left(\frac{R_\odot}{R} \right) \left(\frac{L_\odot}{L} \right). \quad (2.20)$$

For giants with a distinguishable core-envelope structure (envelope mass M_e), one can also use

$$\tau_{th} \sim \frac{U}{L} \sim \frac{GMM_e}{RL} \approx (3.1 \times 10^7 \text{ yr}) \left(\frac{M}{M_\odot} \right) \left(\frac{M_e}{M_\odot} \right) \left(\frac{R_\odot}{R} \right) \left(\frac{L_\odot}{L} \right). \quad (2.21)$$

This is a much longer timescale, but still small compared to the lifetime of a star. We thus consider the star to be in thermodynamic equilibrium most of the time.

Rest mass energy and abundances change on the **nuclear timescale**; relating the fraction of total rest mass energy ϵ and luminosity, we get

$$\tau_{nuc} \sim \frac{\epsilon Mc^2}{L} \sim \epsilon (1.5 \times 10^{13} \text{ yr}) \left(\frac{M}{M_\odot} \right) \left(\frac{L_\odot}{L} \right). \quad (2.22)$$

We can approximate $\epsilon \sim 10^{-3}$, thus $\tau_{nuc} \sim 10^{10}$ yr for the Sun.

The above introduced timescales compare as follows:

$$\tau_{nuc} \gg \tau_{th} \gg \tau_{dyn} \sim \tau_s. \quad (2.23)$$

2.5 Single star evolution

Before binary star evolution can take place, single stars have to form. Depending on their properties at the stage of interaction, the binary system will evolve differently. Therefore, we first want to have a look at single star evolution.

Stars are gas clouds of interstellar medium collapsing under gravity. Under the resulting pressure, nuclear fusion in the core sets in. The star is thus supported by fusion-generated heat against gravity. The evolution depends mostly on its initial mass.

Heat is transported to the surface by radiation or convection. Most main sequence stars keep their equilibrium of gravity, radiation and gas pressure before – only those with a mass exceeding about $0.25 M_{\odot}$ – blowing up to a giant and then shrinking again.

Compared to main sequence stars (or dwarfs), giants are substantially larger in radius up to several hundred solar radii and also brighter in luminosity. We will consider such a giant on the asymptotic giant branch (AGB).

The companion in our binary system is a white dwarf (WD), the hot core (called *remnant*) of a red giant (RG) (its *progenitor*), not able to ignite helium resp. carbon, but still supported against gravity by electron degeneracy pressure. Its mass is well below the Chandrasekhar limit of approx. $1.44 M_{\odot}$ (for non-rotating WD), otherwise (e.g. by accretion of mass from binary) it cannot be supported and undergoes a gravitational collapse, evolving into a neutron star or, beyond $2.5 M_{\odot}$, even a black hole.

2.6 Binary systems

More than half of all stars in the universe are supposed to be in a binary or multiple star system, i.e. close enough to orbit each other around a common barycenter due to gravitational attraction. They originate from a collapsing gas clouds forming several stars at a time by fragmentation. They can further decrease their distances by releasing a component of a multiple star system. On the other side, catching a by-passing object is difficult due to the necessary transfer in angular momentum. However, a higher angular momentum of the interstellar medium collapsing might favor the formation of multiple star systems.

For distinction, the brighter object is called *primary*, the other one *secondary*. This has historical observational reasons, while we differentiate based on their masses with equal effect. Wide binaries show large orbital distances such that they do not affect the evolution of the other, whereas close binaries can do so by transfer of mass.

The orbit of each body can be described as an ellipse as depicted in Figure 2.1. The barycenter of the system then lies at one of the focal points. The distance between the center and either of its two foci is called *linear eccentricity*. The eccentricity of an ellipse is defined as the ratio of the linear eccentricity to the semi-major axis (zero for a circle).

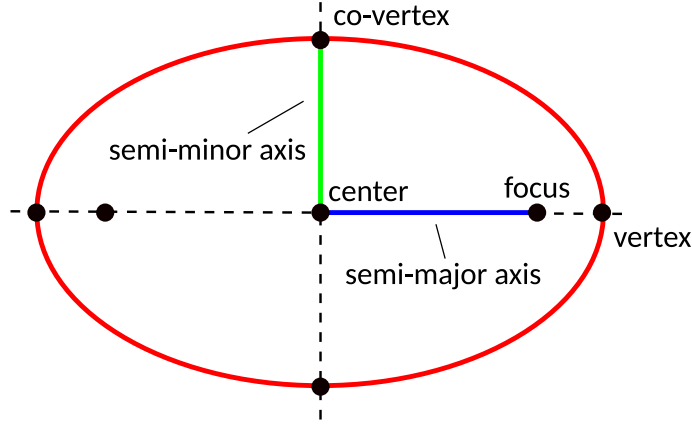


Figure 2.1: Ellipse with annotations. Own work.

Configuration

We consider a binary system with component masses M_1 (primary) and M_2 (secondary), total mass $M_{tot} = M_1 + M_2$ and orbital semi-major axis A . The *mass ratio* is defined as

$$q = \frac{M_2}{M_1}. \quad (2.24)$$

Kepler's laws of planetary motion² state

$$\left(\frac{2\pi}{P}\right)^2 = \omega^2 = \frac{GM_{tot}}{A^3},$$

where P denotes the orbital period and ω the angular frequency.

$$J = \mu r^2 \dot{\Theta} \quad (2.25)$$

is called the *angular momentum*. The total angular momentum is

$$J = \left[\frac{GM_1^2 M_2^2}{M_1 + M_2} A (1 - e^2) \right]^{1/2} \quad (2.26)$$

For solar values and neglecting eccentricity, one gets

$$G^{1/2} M_\odot^{3/2} R_\odot^{1/2} \sim 6 \times 10^{51} \text{ erg s} \quad (2.27)$$

Angular momentum can get transferred within the binary system, as will be treated in Section 2.7.1.

The orbital energy of the system can be written as

$$E_{orb} = E_{pot} + E_{kin} = -\frac{GM_1 M_2}{A} + \frac{GM_1 M_2}{2A} = -\frac{GM_1 M_2}{2A}. \quad (2.28)$$

²At the beginning of the 17th century, they were initially formulated for the motion of planets around the Sun, but can of course be applied to any ideal two-body problem.

Roche lobe

The combined gravitational potential of masses at \mathbf{r}_1 and \mathbf{r}_2 , called *Roche potential*, writes as

$$\Phi_{\text{Roche}}(\mathbf{r}) = -\frac{GM_1}{|\mathbf{r} - \mathbf{r}_1|} - \frac{GM_2}{|\mathbf{r} - \mathbf{r}_2|} - (\boldsymbol{\omega} \times \mathbf{r})^2 \quad (2.29)$$

and is illustrated in Figure 2.2.

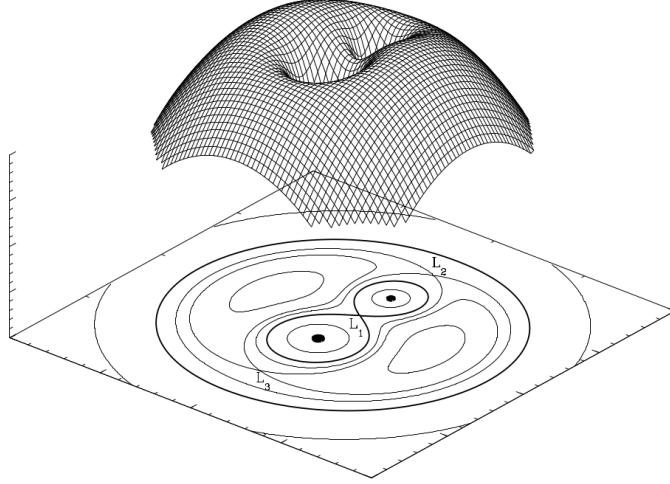


Figure 2.2: Roche potential with a three-dimensional representation, $q = 0.5$. The lines in the plane represent equipotential surfaces, the droplet-shaped areas are the Roche lobes, the larger one belongs to the more massive primary. The points L_1, L_2, L_3 are the Lagrangian points where forces cancel. When the Roche lobe is filled, mass can be transferred to its companion through L_1 (which is not the center of mass). Mass can be expelled to a surrounding disc through L_3 or out of the system through L_2 if both stars' Roche lobes are filled. Figure from [Sluys \[2006\]](#).

We find equipotential surfaces setting $\Phi_n = \text{constant}$. Extrema in the orbital plane are called *Lagrange points*. The first one, L_1 , lies between the two masses. The *Roche lobe* is defined as equipotential surface containing L_1 . The effective radius r_L is the radius of a sphere that contains the same volume as the Roche lobe. Eggleton approximation [[Eggleton, 1983](#)] reads as

$$r_L = \frac{0.49q^{2/3}}{0.69q^{2/3} + \ln(1 + q^{1/3})}, \quad (2.30)$$

which is accurate within 1 % for $0 < q < \infty$. r_L is the value normalized by the orbital separation A , thus *Roche lobe radius* $R_L = Ar_L$. Once the Roche lobe is filled, *Roche lobe overflow* (RLOF) sets in.

2.7 Common envelope phase

The CE is a short phase in the binary star evolution. When the atmosphere of a giant expands, mass can be transferred to the companion, leading to a further expansion of the giant evolving towards its thermodynamical equilibrium. The loss of angular momentum leads to the inspiral, further increasing mass transfer. The companion can no longer accrete the mass, a CE is formed where the two stars orbit in a single, shared envelope. Mass and energy transfer lead to the ejection of the CE. With a decreased separation, the stars may even merge. Paczynski [1976] first described such a CE system, including mass transfer, now they are widely used to explain many observed compact binaries. Besides the state of evolution of the stars, the CEE depends on parameters, including rotation of the envelope and mass ratio, cf. De Marco et al. [2003]. For a complete overview on the topic, see Ivanova et al. [2013].

Classification

There are three different phases according to Podsiadlowski [2012]. These are hard to distinguish due to smooth transitions. Ivanova and Nandez [2016] specified them quantitatively:

- I *Loss of co-rotation.* So far, the companion was on a stable orbit, probably tidally locked to the primary. This orbit now changes into a spiral-in, caused, e.g., by the expansion of the primary (so-called donor) due to its evolution. The change in the orbital separation A is less than one per cent over the orbital period P , $|(\dot{A}P)|/A < 0.01$.
- II *Plunge-in.* Rapid spiral-in and orbital shrink-age, $|(\dot{A}P)|/A \gtrsim 0.1$. The companion plunges into the CE so that finally a substantial part of its mass is outside the companion's orbit.
- III *Self-regulating spiral-in.* The change in orbit is small again, in terms of orbital energy E_{orb} , $|(\dot{E}_{orb}P)/E_{orb}| < 0.01$.

At the end of the evolution, the two stars are closer and have ejected a certain fraction of their envelope. Ivanova and Nandez [2016] identified three possible outcomes:

- binary formation: CE ejected completely, $|(\dot{E}_{orb}P)/E_{orb}| < 0.01$,
- slow spiral-in: CE not fully ejected, rapid mass outflow stopped, $|(\dot{E}_{orb}P)/E_{orb}| < 0.01$,
- merger: orbital separation $< 0.15 R_{\odot}$.

During the CEE, they identified four different processes of ejection:

- pre-plunge-in ejection,
- the outflow during the plunge-in,
- the outflow driven by recombination,
- the ejection triggered by a contraction of the circum-binary envelope.

The unbound envelope material is denoted M_{ej} (*ejected*). Mass becomes ejecta when it gets a positive total energy, while it is bound as long as its total energy is negative.

Mass transfer

When the two components come close enough, i.e. about Roche lobe, they start interacting and mass transfer will set in. Mass from the primary (donor) will start to fill the Roche lobe of the secondary, forming an accretion disk around it.

Since total mass conserved, i.e. $\dot{M}_1 + \dot{M}_2 = 0$, Equation 2.26 for a circular orbit gives

$$J = M_1 M_2 \sqrt{\frac{GA}{M}}, \quad (2.31)$$

thus

$$\dot{J} = 0, \dot{A} = \frac{2(M_1 - M_2)A}{M_1 M_2} \dot{M}_1. \quad (2.32)$$

Since $M_1 \geq M_2$, this means that the orbit is increasing if the primary is gaining mass.

We can define a timescale for mass-transfer

$$\tau_{MT} = \frac{M_e}{\dot{M}} \quad (2.33)$$

Rapid mass transfer is expected if the mass of the giant is more than about 2/3 of the mass of the companion [Eggleton, 2006]. [Rasio and Livio, 1996] identified spiral shock waves and gravitational torques as a mechanism for the transfer of angular momentum from the cores to the gas. The torques act due to *dynamical friction* by a gravitationally interacting mass (the companion in our case), moving through gas (the envelope). A simplified equation for the force resulting from dynamical friction is given by

$$F_{dyn} \sim G^2 \frac{M_2^2 \rho}{v_2^2}, \quad (2.34)$$

with the companion mass M_2 , velocity v_2 and the density of the envelope ρ [Carroll and Ostlie, 2017].

It is initially not clear where this spiral-in will stop: Either the companion merges with the core or finds a stable orbit, depending on the energetic contributions.

2.7.1 Angular momentum

Using the orbital energy, $E_{orb} = -GM_1M_2/2a$, one can find the ratio of the final to the initial orbital angular momentum

$$\frac{J_f}{J_i} = \left(\frac{M_c}{M_1}\right)^{3/2} \left(\frac{M_c + M_2}{M_1 + M_2}\right)^{-1/2} \left(\frac{E_{orb}^f}{E_{orb}^i}\right)^{-1/2} \left(\frac{1 - e_f^2}{1 - e_i^2}\right)^{1/2}. \quad (2.35)$$

Neglecting the initial eccentricity and since $M_c < M_1$, for any final orbital energy state lower than the initial one, one requires angular momentum to be lost.

[Paczyński and Ziółkowski \[1967\]](#) proposed a formalism for the loss of angular momentum in the CEE

$$\frac{J_f - J_i}{J_i} = \gamma \frac{M_1^f - M_1^i}{M_{tot}}, \quad (2.36)$$

where the coefficient γ indicates how many times the specific angular momentum is transferred by the loss in mass. It is in the order of unity and theoretically not well understood yet [[Nelemans et al., 2000](#)].

2.7.2 Energetics

Before considering core and envelope of the primary separately, we need to define them. With this, the CE interaction can be characterized by comparing the change in binding and orbital energy, defining

$$\alpha_{CE} = \frac{E_{bin}}{\Delta E_{orb}}, \quad (2.37)$$

the efficiency of the usage of orbital energy to unbind the envelope, following [De Marco et al. \[2011\]](#). Further energetic contributions, i.e. thermal, recombination and nuclear energy, may also affect the process and may need to be included.

Core criterion

Giant stars have a distinguishable core-envelope structure, i.e. a dense, hot core and a convective envelope. The definition of this boundary is crucial since the binding energy of the envelope is computed by integrating the different energy forms (see following sections) from this core-envelope boundary to the surface of the star and thus depends on it.

Widely used criteria (see for example [de Kool \[1990\]](#)) are based on the abundance of hydrogen, in particular the inner radius with $X = 0.1$, similar to the radius of highest nuclear energy generation. Another criterion is based on the density, minimizing $dm/d \log r$, which has a larger radius.

The choice of the definition of the core also has an influence on the formalism of the binding energy. A smaller core results in a tighter binding of the envelope, yielding a higher binding energy.

Binding energy

As proposed by [De Marco et al. \[2011\]](#), the gravitational binding energy can be expressed as

$$E_{bin} = - \int \frac{Gm}{r} dm = E_{ce} + E_{ee}, \quad (2.38)$$

calculating separately the contributions from the binding core-envelope E_{ce} and the envelope to itself E_{ee} , since we are dealing with a small and dense core (even a point mass in our case) and a less dense and extended envelope. The total mass of the giant star M_1 equals $M_c + M_e$, the core and envelope mass respectively.

The envelope structure parameter λ is introduced approximates all the mass of the envelope at a mass-averaged radius λR . With this,

$$E_{ce} = -G \int \frac{M_c}{\lambda R} dm = -G \frac{M_c M_e}{\lambda R}. \quad (2.39)$$

λ is in the order of unity.

$$E_{ee} = -\frac{G}{2} \int \int \frac{dm dm'}{|\mathbf{r} - \mathbf{r}'|} \quad (2.40)$$

with mass parcels dm and dm' separated by distance $|\mathbf{r} - \mathbf{r}'|$, factor $\frac{1}{2}$ account double counting.

Approximating for $|\mathbf{r}| = |\mathbf{r}'| = \lambda R$,

$$|\mathbf{r} - \mathbf{r}'| = \frac{1}{\lambda R} \sum_{n=0}^{\infty} P_n(\cos \phi) \approx \frac{1}{\lambda R} (1 - (\cos \phi)) \quad (2.41)$$

with the Legendre polynomial P_n to order $n = 1$ ($P_0 = 1$, $P_1 = \cos \phi$), angle between \mathbf{r} and \mathbf{r}' ϕ , symmetry vanishing term on $\cos \phi$.

Thus,

$$E_{bin} \approx -G \frac{M_e \left(\frac{M_e}{2} + M_c \right)}{\lambda R} \quad (2.42)$$

Orbital energy

With gravitational potential

$$\Phi = -\frac{Gm(r)}{r}, \quad (2.43)$$

we find

$$E_{orb} = -G \left[\frac{M_c M_2}{2A_f} - \frac{(M_c + M_e) M_2}{2A_i} \right] \quad (2.44)$$

and thus

$$-G \frac{M_e \left(\frac{M_e}{2} + M_c \right)}{\lambda R} = -\alpha_{CE} G \left[\frac{M_c M_2}{2A_f} - \frac{(M_c + M_e) M_2}{2A_i} \right], \quad (2.45)$$

with the efficiency of unbinding in CE α_{CE} .

Thermal energy

The envelope structure parameter λ according to [Webbink \[2008\]](#) is not only the mass-averaged radius of the envelope, it also accounts for the *thermal energy* of the initial envelope. The thermal energy, the energy stored in the gas due to its thermal motion, may also affect the dynamics. The virial theorem (cf. Section 2.1), assuming an ideal mono-atomic gas, relates kinetic energy E_{kin} to the binding energy as

$$2E_{kin} + E_{bin} = 0. \quad (2.46)$$

[Webbink \[2008\]](#) extended this expression for the envelope by a term to account for its thermal energy:

$$2E_{kin,env} + 4\pi R_c^3 P_c + E_{bin,env} = 0. \quad (2.47)$$

Recombination energy

Due to the temperature, we expect the gas inside the star to be fully ionized.

As the envelope expands, the gas cools down, allowing the ionized plasma to recombine. During this process, recombination energy ΔE_{rec} is released, which can further unbind mass of the envelope. It is not clear how much of the released recombination energy can be used to do so, as some of it is expected to be radiated away, especially in the optically thin, i.e. low opacity, outer region of the envelope, close to the photosphere.

Following [Ivanova and Nandez \[2016\]](#), one can calculate the recombination energy stored in the ionized matter of the envelope as

$$\Delta E_{rec} \approx 2.6 \times 10^{46} \text{ erg s} \frac{M_e}{M_\odot} (X f_{HI} + Y f_{HeII} + 1.46 Y f_{HeI}), \quad (2.48)$$

where X denotes the hydrogen and Y the helium mass fraction and the three main contributions ionized hydrogen, HI , singly ionized helium, $HeII$, and doubly ionized

hydrogen, *HeIII*. Assuming complete recombination, $\Delta E_{rec} \approx 3 \times 10^{46} \text{ erg } \frac{M_e}{M_\odot}$. Comparing this with the binding energy one can see that the total energy is positive for stars with $R \gtrsim 127 \frac{R_\odot}{\lambda}$. Thus, if the recombination takes place and energy is not simply radiated away, the envelope can get unbound.

Ivanova and Nandez [2016] propose a *recombination radius* r_{rec} , defined as the radius at which the specific recombination energy exceeds the local specific potential energy $\epsilon_{grav} = -\frac{GM}{r} = -1.9 \times 10^{15} \text{ erg g}^{-1} \left(\frac{M}{M_\odot} \right) \left(\frac{R}{R_\odot} \right)^{-1}$. Due to the mass loss of the envelope, this radius gets smaller during the binary simulation.

As internal energy, the ideal gas possesses only thermal energy, the OPAL EOS further accounts for ionization energy. For clarity in notation and comparison of values, we will refer to it as E_{therm} for the ideal gas EOS, leaving e_{int} undefined.

Nuclear energy

The nuclear energy stored due to the conversion of hydrogen into helium is

$$\epsilon_{nuc} = 0.007mc^2 \sim 6 \times 10^{18} \text{ erg g}^{-1} \sim 1 \times 10^{52} \text{ erg } \frac{m}{M_\odot} \quad (2.49)$$

whereas gravitational energy released by mass m falling (from infinity) on a star with mass M and radius R

$$\Delta E_{grav} = \frac{GMm}{R} \sim 4 \times 10^{48} \text{ erg } \left(\frac{m}{M_\odot} \right) \left(\frac{M}{M_\odot} \right) \left(\frac{R}{R_\odot} \right)^{-1} \text{ erg}. \quad (2.50)$$

The nuclear energy, however, is released on a time scale of about $\tau_{nuc} \sim 10^{11} \text{ yr}$, leading to an annual energy rate of $\epsilon_{nuc}\tau_{nuc} \sim 1 \times 10^{41} \text{ erg yr}^{-1} \frac{m}{M_\odot}$.

Further aspects

The presence of ionized species in principle also requires magnetohydrodynamics. However, Ohlmann [2016] found no significant change in the outcome. Glanz and Perets [2018] propose winds to finally unbind the expanded matter of the envelope. Soker [2017] proposes jets as a mass transport mechanism. They might occur when an accretion disk is present around the secondary, feeding the jet. However, the formation of jets is not yet well understood. If there are non-conservative forces such as the viscous force acting in the accretion disk, the gas might reach such high temperatures that angular momentum and orbital energy can be radiated away. We might expect this for very high-mass secondaries. In the accretion disk, magnetic fields might act more efficiently than in the common envelope, also extracting energy and angular momentum from the gas.

3 Numerical Methods

Code

We are using AREPO [Springel, 2010] with a moving unstructured mesh based on the Voronoi tessellation, which is illustrated in Figure 3.1. We can set the mesh-generating points freely in principle. If we choose them stationary, we obtain an ordinary Eulerian method, i.e. looking at the mass distribution at fixpoints, with second-order accuracy. If we connect them to mass elements, we are dealing with a Lagrangian formulation, that does not suffer from mesh effects, making it fully Galilean-invariant, unlike ordinary Eulerian schemes. By redefining the cells, we can adjust resolution according to simple criteria (adaptive mesh refinement).

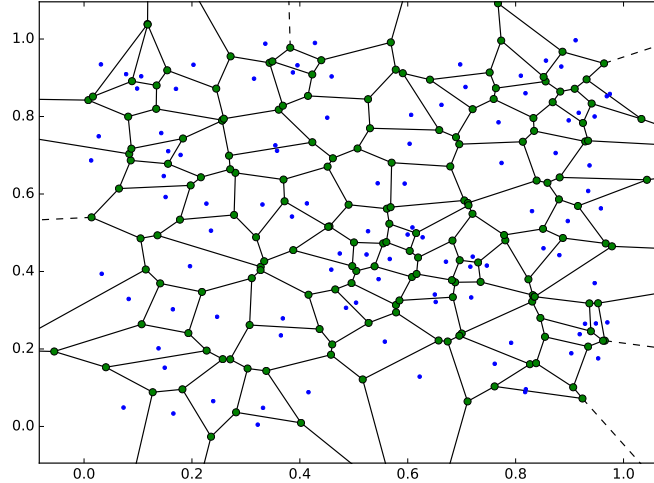


Figure 3.1: Voronoi tessellation for a set of 100 random points. The mesh-generating points are shown in blue, the points spanning the cells in green. The cells consist off all points closer to the therein included mesh-generating point than to any other. Own work.

The equations of hydrodynamics (cf. Section 2.1) are solved on this mesh with a finite volume approach, based on a second-order unsplit Godunov scheme¹ with a Riemann solver². This allows an accurate treatment of shocks, rarefaction waves

¹In 1959, S. K. Godunov was the first to introduce an exact Riemann solver for hyperbolic partial differential equations such as the Euler equations. It is basically first order accurate in space and time, but can be used to develop higher-order schemes.

²The *Riemann problem* is an initial value problem with some conservation equation and constant initial data except for a single discontinuity.

and contact discontinuities.

The routine first loads the initial conditions and does a domain decomposition, followed by the calculation of the gravitational forces and the Voronoi mesh. The main loop determines a new time-step and does the first gravitational half-kick, then calculates gradients, vertex velocities and the hydro flux. The (de-)refinement of the cells is done and particles are assigned. The timebins are updated, activating only particles relevant for this step and then starts again for the second gravitational half-kick. The OPAL EOS comes as a table on a temperature-density grid with an interpolation code.

Simplifications

Numerics cannot solve all problems, accounting for and resolving all physical mechanisms existent. Instead, we need to identify the important ones. Since [Ohlmann \[2016\]](#) found no significant difference during his runtime, we neglect magnetic fields. Considering the timescales (Section 2.4) involved in our problem, we neglect nuclear burning, i.e. there is no heating at the core, and we do not treat radiation transport, since $\tau_{nuc} \gg \tau_{th} \gg \tau_{dyn}$.

Core model

Because of the six orders of magnitude difference in time scales, the inner part of the star would require time-steps about this factor smaller than in the outer part, which is not computationally feasible. In order to obtain a stable hydrostatic atmosphere, [Ohlmann \[2016\]](#) uses a modified Lane-Emden equation. The central region is cut at a certain relative cut-off radius r_{cut} and replaced by a point mass, the profile is continued to the center in a stable way.

The point mass interacts only gravitationally, its potential is modified with the softening kernel

$$\Phi_{dm}(r, h) = -\frac{G}{r} \begin{cases} \frac{14}{5}u - \frac{16}{3}u^3 + \frac{48}{5}u^5 - \frac{32}{5}u^6 & 0 \leq u < \frac{1}{2} \\ -\frac{1}{15} + \frac{16}{5}u - \frac{32}{3}u^3 + 16u^4 - \frac{48}{5}u^5 + \frac{32}{15}u^6 & \frac{1}{2} \leq u < 1 \\ 1 & u \geq 1, \end{cases}$$

with $u = \frac{r}{h}$ and softening length $h = r_{cut}/2.8$.

The equations of hydrostatic equilibrium have to be adapted to account also for the core mass.

4 Initial Models

Before simulating the dynamical spiral-in in a binary system, we need to determine our initial conditions. They need to be set carefully, making sure no perturbations due to an unresolved equilibrium or numerical effects substantially influence the following dynamics.

The main effort has to be put in the AGB star model. For the binary setup, we will add a white dwarf orbiting around it.

The crucial part is to obtain a steady state for the weakly bound convective atmosphere around the core. The first step thus consists of finding a suitable model, then mapping the giant on our grid.

According to [Ohlmann \[2016\]](#), criteria to be matched are:

1. The deviations from the initial profiles of pressure and density distributions should be small.
2. The hydrostatic equilibrium should be reached.
3. For convectively stable atmospheres, Mach numbers in the atmosphere should be very small. For convectively unstable models, a steady state should be reached.
4. The potential energy of the system should be constant in order to exclude the presence of pulsations.

4.1 Stellar profile

For the stellar evolution to the desired stage, we use the one-dimensional stellar evolution code MESA (*Modules for Experiments in Stellar Astrophysics*) by [Paxton et al. \[2010\]](#). The most important parameters are the zero-age main sequence (ZAMS) mass and initial metallicity.

We want to consider models with a ZAMS mass of $1.2 M_{\odot}$ and $2.5 M_{\odot}$ with initial metallicity $X = 0.02$. The evolution is exemplarily shown in Figure 4.1.

The star was evolved until the radius in the AGB stage became larger than the largest radius of the RG stage. If the same radius was reached in the RG evolution, one might expect a CE in this earlier stage already. The properties of our two models are shown in Table 4.1.

The $1.2 M_{\odot}$ ZAMS mass model lost a substantial fraction of its mass during evolution, resulting in an $0.96 M_{\odot}$ AGB star. The main reason for this mass loss are strong winds due to radiation pressure that act at the surface of giants where the

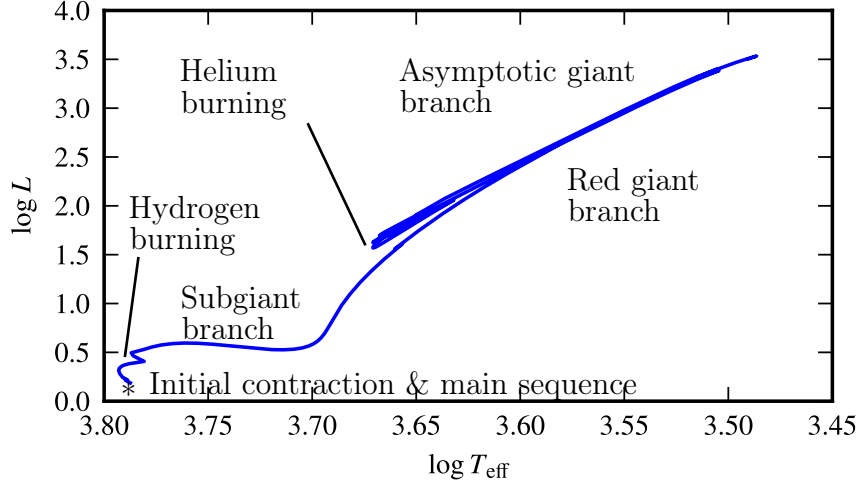


Figure 4.1: Hertzsprung-Russell diagram of the $1.2 M_{\odot}$ model. The evolution goes from bottom left (main sequence) to top right, from where our AGB model is taken.

Table 4.1: Parameters of profiles from MESA.

model	model age	radius	mass	τ_{dyn}	τ_{th}	τ_{nuc}
$1.2 M_{\odot}$	6.3×10^9 yr	$173 R_{\odot}$	$0.97 M_{\odot}$	267 d	47 yr	3.6×10^6 yr
$2.5 M_{\odot}$	7.7×10^8 yr	$99 R_{\odot}$	$2.48 M_{\odot}$	72 d	849 yr	1.4×10^7 yr

atmosphere is only tightly bound. For the designation, we will refer to its ZAMS mass.

4.2 Mapping

The 1D profile from MESA cannot be used for our 3D AREPO grid without prior considerations. Its high radial resolution has to be adapted for a 3D setup, trying to resolve the essential gradients while introducing 3D effects such as convection. We need to find a stable representation with the inner dense region replaced by a point mass.

Around this point mass, the mass is assigned to Voronoi cells, following the mass distribution inside the star with spherical shells according to the HEALPix (Hierarchical Equal Area isoLatitude Pixelization) grid [Górski et al., 2005].

The central point mass also simplifies the distinction of core and envelope for the analysis, but might not allow a treatment of the full hydrodynamics of the CE phase (cf. Section 2.7.2). Especially after the plunge-in, when the two cores are close, the unresolved matter of the envelope may prevent further evolution.

The stellar structure equations are integrated to be solved for the modified profile due to the point mass representing the core. This aims at profiles for density and pressure. Due to the EOS, thermodynamic quantities might vary a bit, affecting zones of convection in particular. In order to conserve those, the difference between temperature gradient and adiabatic temperature gradient can be integrated. However, this affects the other quantities again. We therefore prefer to validate convection by comparing to a modified temperature gradient, see Section 4.6. Outside the star, additional mass is assigned to the cells on the grid in order to allow for computation of fluxes.

Models with different cut-off radii at the inner core were tested. The aim is to decrease it, resolving more of the envelope's mass on the grid. For the tested total resolution, 10 and 20 % cut-off radius revealed similar Mach numbers as the 5 % model. Below that (tested for 2.5 %), for the given total resolution (number of cells), the hydrostatic equilibrium is no longer resolved in a sufficient way. Thus, in the following study, we will use a 5 % cut-off radius.

4.3 Relaxation

Mapping the stable 1D profiles onto the 3D grid may introduce numerical errors. A relaxation is performed for ten acoustic timescales to make sure that the giant is stable before the interaction with a companion. Velocities are damped for half of the time, the rest of the time is for verification of the stability, according to [Ohlmann \[2016\]](#):

$$\mathbf{v}(t) = \mathbf{v}_0 e^{-t/\tau}. \quad (4.1)$$

Until $t_1 = 2\tau_{dyn}$, velocities are damped on a tenth of the dynamical timescale ($\tau_1 = \tau_{dyn}/10$), with a transition to damping on the dynamical timescale ($\tau_2 = \tau_{dyn}$) at $t_2 = 5\tau_{dyn}$, after which velocities are no longer damped.

$$\tau(t) = \begin{cases} \tau_1 & t < t_1 \\ 1/\tau_1 * \left(\frac{\tau_1}{\tau_2}\right)^{\frac{t-t_1}{t_2-t_1}} & t_1 < t < 5t_2 \\ \infty & t > t_2. \end{cases}$$

Figure 4.2 shows the profiles of the initial conditions.

During the run, cells are refined and de-refined in order to keep the mass per cell about constant. Besides, the boundaries of the atmosphere need to be resolved in order to maintain a stable model.

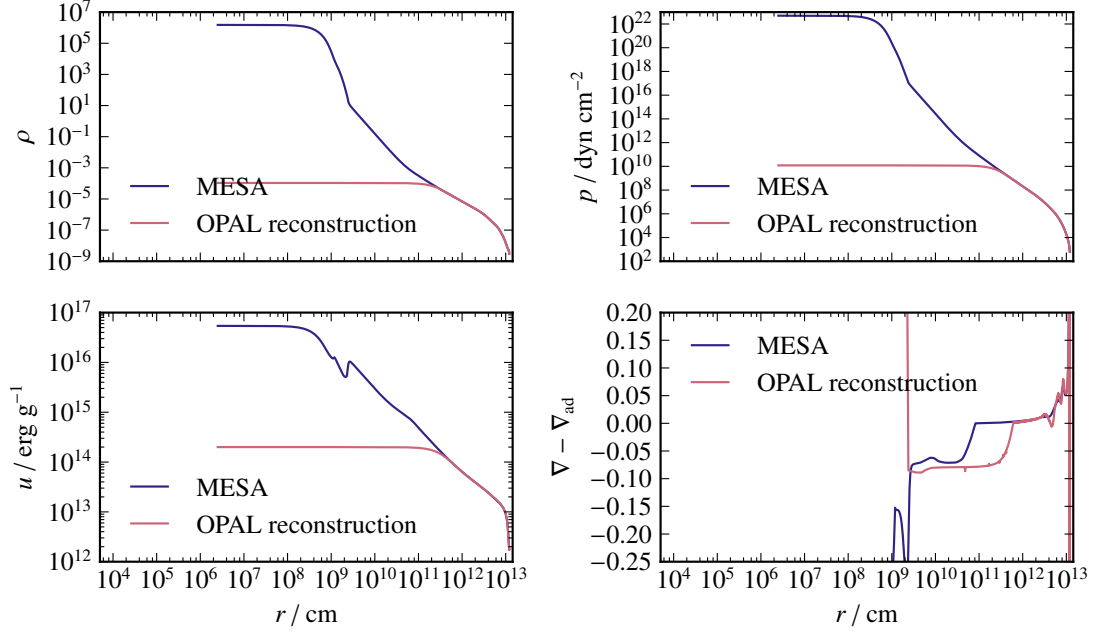


Figure 4.2: Profiles of density ρ , pressure p , specific internal energy u and difference in gradients $\nabla - \nabla_{ad}$ of the initial conditions.

4.4 Resolving the atmosphere boundaries

Simulations with AGB stars so far encountered problems setting up a stable atmosphere, cf. [Ohlmann \[2016\]](#). Of particular interest are the boundaries of the atmosphere, i.e. the softening length around the core and the surface of the star. Increasing the total resolution does not bring stability, and computational resources set limits. We thus perform a more detailed resolution study.

4.4.1 Resolving pressure scale height

One difficulty in the setup of the AGB star is the equilibrium at the surface. We thus define a refinement criterion that resolves the pressure scale height at the outer part of the atmosphere.

Integration of Equation 2.6 for an atmosphere, using the ideal gas law, leads to the pressure dependence of height z

$$dP = -\rho g dz. \quad (4.2)$$

One can now define the *pressure scale height* as

$$H_P \equiv -\frac{dr}{d \ln P} = -P \frac{dr}{dP} = \frac{P}{\rho g}. \quad (4.3)$$

Requiring 5 cells within the pressure scale height at the surface, computational costs triple. These will further increase with the strong dynamics of the binary simulation, so instead of the pressure scale height, we investigate on the softening length.

4.4.2 Resolving the softening length

Gravitational energy is converted to total energy of the gas primarily around the cores, also within the softening length of their gravitational interaction. Thus, we need to resolve the softening length around the point masses, requiring a certain number of cells in the radial direction. This seems crucial: For [Ohlmann \[2016\]](#), 20 cells within the softening length $h = r_{\text{cut}}/2.8$ are sufficient for a stable model of a RG stars and to resolve the energy conversion properly, whereas with this resolution our AGB model first contracts during the relaxation before expanding and blowing away a substantial fraction of its atmosphere. This instability, however, develops at the center of the star, a decrease in density can be observed at any radius. Increasing the resolution to 40 cells considerably increases stability. As can be seen in Figure 4.3, Mach numbers and the imbalance in the equilibrium within the star are reduced by almost an order of magnitude. Due to low density and pressure, the values outside of the star differ significantly, but they are not meaningful.

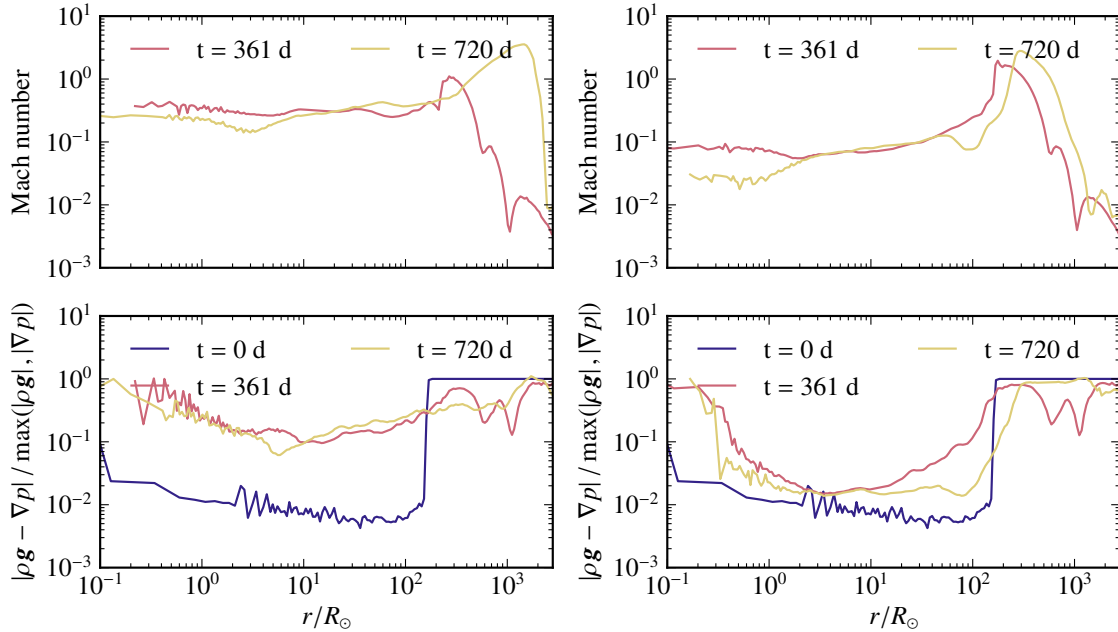


Figure 4.3: Comparison of softening length resolution. On the left, it was resolved with 20 cells, on the right with 40 cells. Both have a total resolution of 2 million cells. Mach numbers (top) within the star are reduced by almost an order of magnitude, just as the imbalance in the equilibrium (bottom).

Further increasing the resolution to 60 cells does not have a considerable effect:

Mach numbers as well as the imbalance in the equilibrium are not further improved.

4.5 $1.2 M_{\odot}$ model resolution study

For the $1.2 M_{\odot}$ model we want to investigate on the effect of resolution. Choosing a total number of cells $N = 6.75 \times 10^6$, instead of $N = 2 \times 10^6$ in our reference run, improves the resolution by 50 % along each axis of the box. Figure 4.4 shows the mass (density) profile for the higher resolution relaxation. The differences between Mach numbers and equilibrium can be improved.

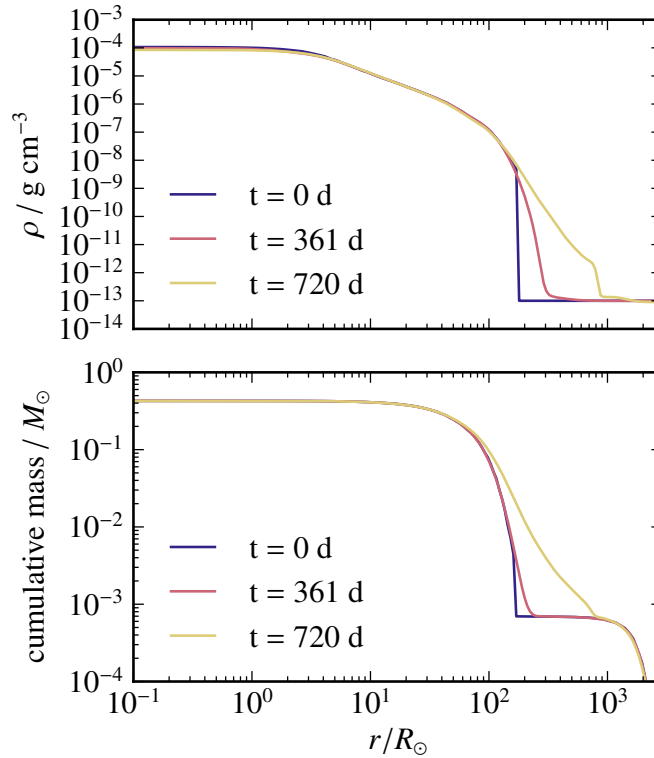


Figure 4.4: Density profile of the relaxation run

Although energy conservation for the lower resolution model reveals a total error of 11 %, the errors regarding potential or internal energy are considerably higher and can be improved by a higher resolution. The values are listed in Table 4.2. An even higher number of cells $N = 10 \times 10^6$ was tested, leading to only marginally smaller errors.

For the $2.5 M_{\odot}$ model, the errors are already sufficiently small, thus no higher resolution is necessary.

Table 4.2: Energy conservation for the $1.2 M_{\odot}$ model and different resolutions.

N	$\Delta E_{pot}/ E_{pot}^i $	$\Delta E_{kin}/ E_{pot}^i $	$\Delta E_{in}/ E_{pot}^i $	$\Delta E_{tot}/ E_{pot}^i $
2×10^6	-0.43	0.00	0.32	-0.11
6.75×10^6	0.03	0.00	-0.02	0.02

4.6 Influence of the EOS

Recombination takes place at lower temperatures. Since giant profiles range to lower densities and temperatures, the difference between the ideal gas and the OPAL EOS is important for our models.

The envelope is expected to be convectively unstable. However, the reconstruction of the stellar profile in case of the ideal gas EOS does not account for the ionization energy from the MESA model; as internal energy, only thermal energy is stored. The difference in the temperature gradient $\nabla - \nabla_{ad}$ is lowered by a mean value of 0.05, $\nabla - \nabla_{ad} < 0$ within the stellar interior. It is thus stable against convection (Schwarzschild criterion, cf. Section 2.2).

In case of the OPAL model, $\nabla - \nabla_{ad} \sim 0$ within the star, thus convection can arise. The difference can be seen for the relaxation of the ideal gas compared to the OPAL EOS in Figure 4.5.

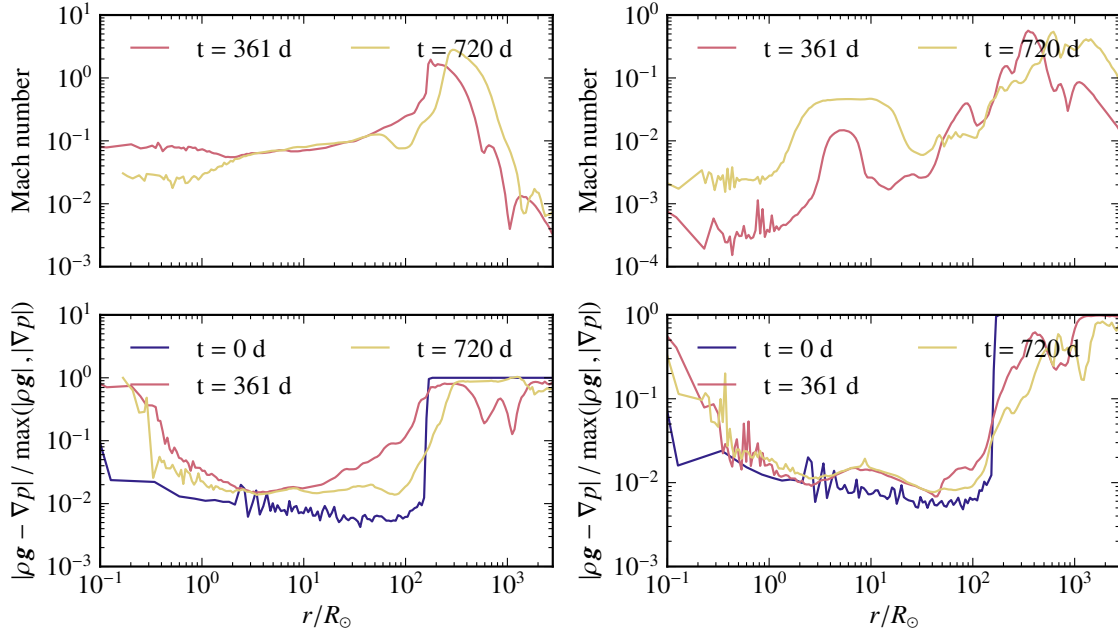


Figure 4.5: Comparison of ideal gas and OPAL EOS. The Mach numbers and difference in hydrostatic equilibrium are shown for the OPAL model with resolution $N = 6.75 \times 10^6$ on the left and the ideal gas model with resolution $N = 2 \times 10^6$ on the right.

Figure 4.6 shows the Mach numbers at the end of the OPAL relaxation with resolution $N = 6.75 \times 10^6$.

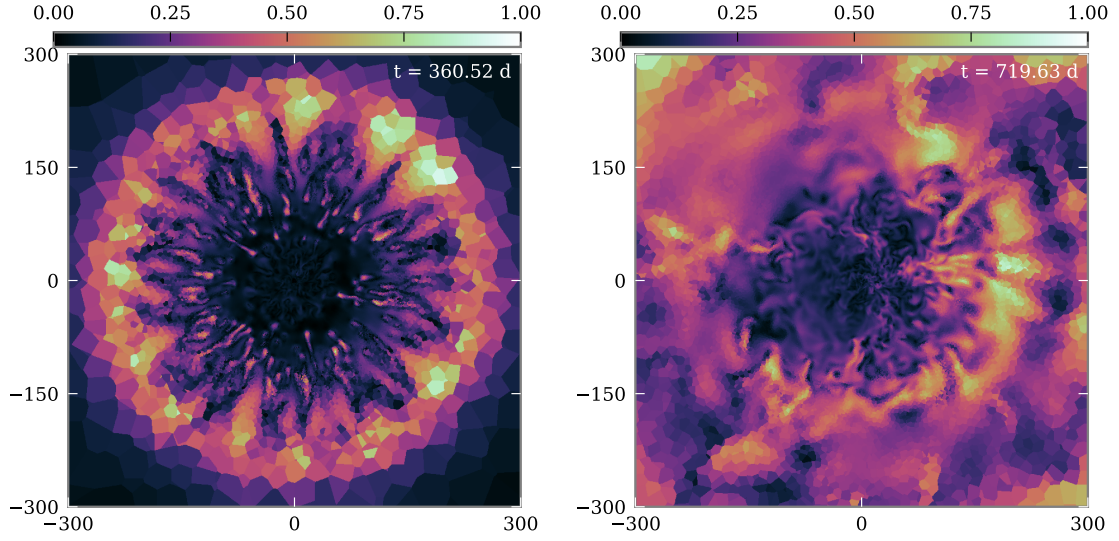


Figure 4.6: Mach plots of $1.2 M_{\odot}$ OPAL relaxation simulation with resolution $N = 6.75 \times 10^6$. The left plot shows convection at the moment when damping is stopped, the right one after five more acoustic timescales.

4.7 Results

With an increased resolution of the softening length around the giant core, both models are stable. For the $1.2 M_{\odot}$ model, maximum Mach numbers inside the star are around 0.11, which is also the mean Mach number on the grid; for the $1.2 M_{\odot}$ model it is 0.07.

The deviations of the energy during the relaxation are shown in Table 4.3.

Table 4.3: Relative deviations of the energy during the relaxation in units of 10^{-2} . The $1.2 M_{\odot}$ OPAL model has resolution $N = 6.75 \times 10^6$, the others $N = 2 \times 10^6$.

model	$\Delta E_{pot}/ E_{pot}^i $	$\Delta E_{kin}/ E_{pot}^i $	$\Delta E_{in}/ E_{pot}^i $	$\Delta E_{tot}/ E_{pot}^i $
$1.2 M_{\odot}$ ideal gas	-5.4	0.0	5.6	0.2
$1.2 M_{\odot}$ OPAL	3.3	0.4	-2.2	1.6
$2.5 M_{\odot}$ ideal gas	-1.2	0.0	1.4	0.2
$2.5 M_{\odot}$ OPAL	-1.9	0.2	2.1	0.3

Considering the criteria for stability stated at the beginning of this chapter, the deviations from the initial pressure and density distributions are small, the mass

expanding beyond the initial radius is about 1 %. The mean difference of both sides of the hydrostatic equilibrium equation are about 2 % for the OPAL models and about 1 % for the ideal gas EOS models. Mean Mach numbers on the grid are 0.10 for the OPAL models and about 0.01 for the ideal gas EOS models. The convection reaches a steady state. Both the differences in the hydrostatic equilibrium and the Mach numbers are mass-averaged quantities. We can exclude the presence of pulsations, the potential energy of the system is constant within the error.

4.8 Model parameters

The parameters of the AGB models to be used for the CE simulation are listed in Table table:spacagb.

Table 4.4: Parameters of the AGB star models.

model	M_1	M_c	M_e	R	r_{cut}
1.2 M _⊙	0.97 M _⊙	0.56 M _⊙	0.42 M _⊙	173 R _⊙	8.7 R _⊙
2.5 M _⊙	2.5 M _⊙	0.5 M _⊙	2.0 M _⊙	99 R _⊙	4.9 R _⊙

5 Common envelope simulation with $1.2 M_{\odot}$ primary

In this chapter, a $1.2 M_{\odot}$ AGB star primary (ZAMS mass, $0.97 M_{\odot}$ at our stage of evolution) with radius $173 R_{\odot}$ is used to perform a simulation of the hydrodynamics of CEE with a less massive white dwarf companion star.

Due to the setup, we are only able to simulate the second of the three phases from Section 2.7, the plunge-in (fast spiral-in). The first phase, the loss of co-rotation, would require a long relaxation and many orbits starting from the Roche lobe orbit without a noticeable loss in orbital separation, which computationally is not feasible. Instead, we set a certain degree of co-rotation χ as an initial condition for the spiral-in and place the companion inside the Roche lobe. The third phase, the self-regulating spiral-in, is discussed in the results.

The terms *gravitational* and *potential* are used synonymously since gravitation is the only potential we are dealing with. The secondary and the core of the primary are referred to as *cores* in contrast to the *envelope*, the atmosphere of the primary.

5.1 Setup

The relaxed model (for parameters, see Section 4.8) is inserted into a box large enough for the expelled matter not to leave the box during the runtime. A companion with a certain mass M_2 , so that the mass ratio $q = \frac{M_2}{M_1} < 1$, i.e. less massive than the primary, is added as a point mass at a certain distance in x -direction $A_i = p R_L$, $p < 1$, i.e. inside the Roche lobe radius, but well above the surface of the star, making sure the interaction since entering the Roche lobe is negligible. The binary is rotating with a frequency $f = \sqrt{GM_T/d^3}$ preserving orbital separation. The atmosphere is rotating with a co-rotation of $\chi = 95\%$ as an initial perturbation for the spiral-in.

The time from the start of the simulation to the start of the plunge-in depends on the initial separation, so choose it consistently at a certain percentage of the Roche lobe distance for our simulations, as long as it is well above the surface of the star. We use an initial separation of $A_i = 0.6 R_L$, corresponding to $236 R_{\odot}$, about one third larger than the radius of the primary.

We terminate our simulations when the unbound mass fraction stagnates. However, simulations of such long runtimes do accumulate errors that need consideration.

A list of all models used in this chapter is given in Table 5.1. The denotation consists of the EOS ('Op' for OPAL, 'Id' for ideal gas), followed by the ZAMS mass in units of M_{\odot} , the resolution n (number of particles), the mass ratio $q = \frac{M_2}{M_1}$ and the relative

initial separation compared to the Roche lobe radius $p = \frac{A_i}{R_L}$).

Table 5.1: Setups for binary runs with $1.2 M_\odot$ AGB primary.

Model	EOS	N	q	p
Id1.2n2e6q50p60	ideal gas	2×10^6	1/2	0.6
Op1.2n6.75e6q50p60	OPAL	6.75×10^6	1/2	0.6
Id1.2n2e6q25p60	ideal gas	2×10^6	1/4	0.6
Op1.2n6.75e6q25p60	OPAL	6.75×10^6	1/4	0.6
Id1.2n2e6q75p60	ideal gas	2×10^6	3/4	0.6
Op1.2n6.75e6q75p60	OPAL	6.75×10^6	3/4	0.6

5.2 Reference run

A first simulation with a WD secondary ($q = 0.5$) was conducted for both the ideal gas and the OPAL EOS, the latter accounting for recombination effects as well. Since recombination takes place when the ionized gas cools down, it also acts on expelled matter in outer regions after the spiral-in, thus the OPAL run is expected to take longer than the ideal gas EOS runs. The total energy of the system is positive, the envelope thus may become entirely unbound. The physical timescale of the ideal gas (OPAL) EOS simulation is about 2000 d (4000 d). The simulations took 1.1×10^6 (2.1×10^6) time-step integrations, but not all cells require the smallest time-steps. We can follow about 70.5 (112.5) binary periods, thereof 66.5 (108) orbits after the end of the plunge-in. Figure 5.1 shows the orbital evolution of the OPAL reference run.

The Id1.2n2e6q50p60 (Op1.2n6.75e6q50p60) run starts with an initial orbital period of 332 d (346 d), a difference that is due to a slightly higher mass of the ideal gas model, leading to a higher angular frequency. The dynamical timescale of the $1.2 M_\odot$ AGB model is 30 d. A first shock wave forms due to the higher speed of the secondary compared to envelope (the acoustic timescale is 72 d) and a tidal deformation towards the secondary can be observed, accreting mass onto the secondary and enclosing it after about 61 d (68 d). At that time, the plunge-in phase starts, characterized by a loss in orbital separation per period ($|(\dot{a}P_{orb})|/a$) of more than 10 %; the eccentricity becomes as high as $e \sim 0.8$. Another shock is caused when the first shock hits the moving AGB core, leading to an expansion of the envelope. 414 d (572 d) after the start of the plunge-in, the loss in orbital distance falls below the threshold value and this phase is terminated at an orbital distance of $52 R_\odot$ ($60 R_\odot$) and period 41 d (53 d). However, at the end of the run, i.e. when the unbound mass fraction stagnates, after 2000 d (4000 d), the remaining orbital distance is only $31 R_\odot$ ($39 R_\odot$) and period 19 d (29 d). The final orbit has a low eccentricity of $e \approx 0.04$ (0.01). Figure 5.2 shows the dynamics as a series of density plots for the OPAL reference run in the x - y -plane. Since the dynamics is similar for the two

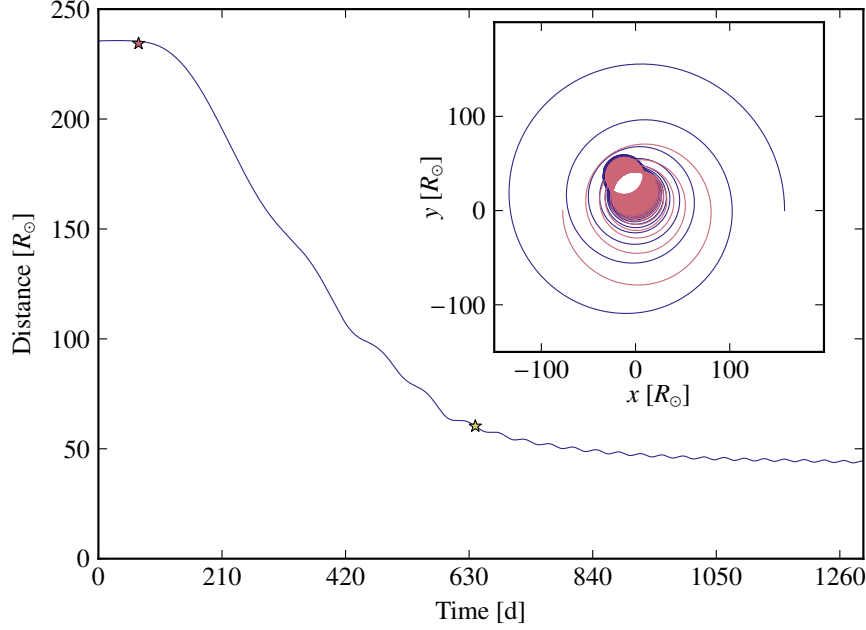


Figure 5.1: Orbit of the Op1.2n6.75e6q50p60 reference run. The orbital distance with oscillations due to eccentricity is plotted over time, the stars mark the start resp. the end of the plunge-in phase. The inset shows the orbit of the primary in red and the orbit of the secondary in blue.

different EOS runs, we will exemplarily discuss the OPAL simulation. One can see two spiral arms moving outwards. One results from the shock when the accretion stream hits itself and is fed by the accreted mass around the secondary. Shortly after, a tidal arm moves out on the opposite side of the envelope. Since mass is removed from its surface, the remaining atmosphere starts its expansion towards a new hydrostatic equilibrium. Due to the inspiral, the orbital frequency increases, and after one orbit, shear instabilities arise within the spiral arms. The spiral arms themselves move outwards with higher velocities, too. It happens that subsequent shock layers hit previous layers. When the second arm hits the first one after $13/8$ orbits (400 d) at roughly $700 R_{\odot}$ distance from the center of mass, shear instabilities arise between the two layers. After four orbits (600 d), the radius at which consecutive layers hit has shrunk to about $200 R_{\odot}$ and instabilities form even inside this radius where density is increased due to the expansion of the primary. At outer radii, the instabilities between consecutive layers rather overlap than mix, while the two cores still create new shock layers and preserve the spiral structure, unlike in the case of a more compact RG simulation by [Ohlmann \[2016\]](#), where after 120 d the spiral structure is not visible anymore.

Figure 5.3 shows the Mach numbers for the OPAL reference run in the x - y -plane. The regions between the supersonic shocks are transsonic, outside of the spiral structure it is supersonic due to the rotation in the setup. Velocities differ where instabili-

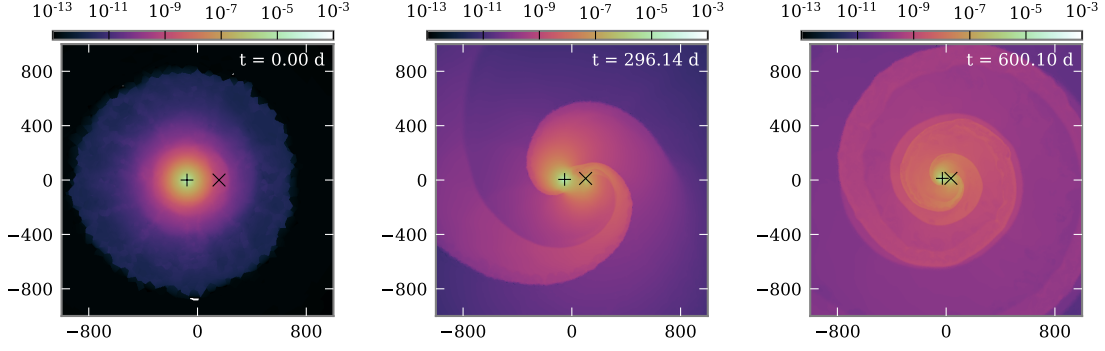


Figure 5.2: Density plots of Op1.2n6.75e6q50p60, at the beginning of the simulation and after one resp. four orbits. Shown is a slice of the x - y -plane, in which the orbit of the cores lies, with spatial scale in units of R_{\odot} from the center of mass, color scale from 10^{-13} to $10^{-3} \text{ g cm}^{-3}$. The core of the primary is marked by a +, the secondary by a \times .

ties form, resulting in shear flows and reduced velocities. Furthermore, the turbulent convection caused by the instabilities changes energy transport.

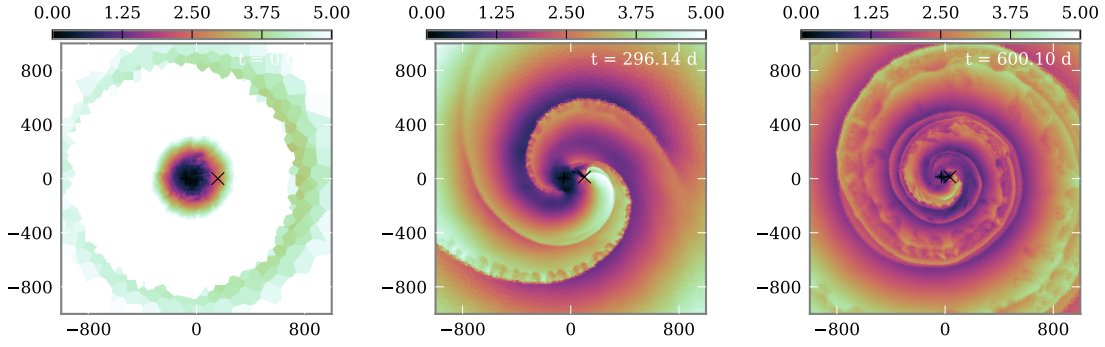


Figure 5.3: Mach numbers for Op1.2n6.75e6q50p60, at the beginning of the simulation and after one resp. four orbits, in the x - y -plane, in which the orbit lies. The color scale ranges from 0 to 5. The core of the primary is marked by a +, the secondary by a \times .

Instabilities arise in the perpendicular plane as well. Figure 5.4 shows plots of the Mach number in the x - z -plane, perpendicular to the orbit of the cores. The spherical supersonic and vertical low-Mach structure is due to the rotating setup again. The spiral arms are formed as sharp angular segments of $\pi/3$ of polar angle during the first orbit. Later layers have a more spherical cross-section due to the plunge-in. The spiral structure then extends to an angular segments of $5/6\pi$ of polar angle. Figure 5.5 shows the orbital distance of the reference runs over time. As described before, the companion of the ideal gas reference run is slightly faster, thus angular momentum is transferred faster, leading to a faster spiral-in compared to the OPAL

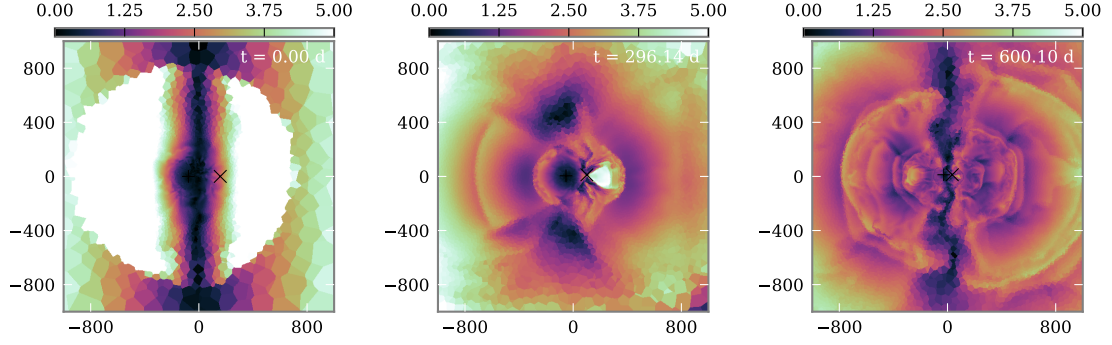


Figure 5.4: Mach numbers for Op1.2n6.75e6q50p60 in the x - z -plane, perpendicular to the orbit. The core of the primary is marked by a $+$, the secondary by a \times .

run.

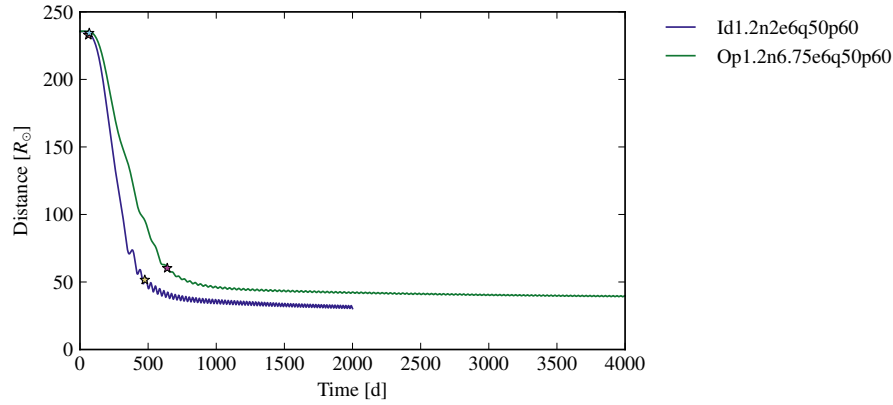


Figure 5.5: Orbital distance of the $1.2 M_{\odot}$ primary reference runs over time. The stars mark the start resp. the end of the plunge-in phase.

Table 5.2 shows the comparison of orbital parameters between the ideal gas and OPAL EOS reference run for the total run and the plunge-in phase separately.

5.3 Angular momentum

Angular momentum is transferred from the cores to the envelope, mainly during the plunge-in, cf. Figure 5.6. The error on the angular momentum during that time is less than 0.5 %.

The values for the γ -formalism according to Nelemans et al. [2000] (cf. Section 2.7.1) considering the total run are listed in Table 5.3. The parameter γ gives the reciprocal of an efficiency of unbinding by angular momentum. Directly after the plunge-in, less mass is unbound with the same value for the ejected angular momentum. This yields higher values of $\gamma = 4.0$ (OPAL) resp. $\gamma = 5.4$ (ideal gas EOS).

Table 5.2: Orbital parameters of the $1.2 M_{\odot}$ AGB primary reference runs. The plunge-in takes 572 d (OPAL) resp. 414 d (ideal gas EOS).

model	considering	A_i	A_f	P_f
Id1.2n2e6q50p60	plunge-in	233 R_{\odot}	52 R_{\odot}	41 d
Id1.2n2e6q50p60	total run	236 R_{\odot}	31 R_{\odot}	19 d
Op1.2n6.75e6q50p60	plunge-in	234 R_{\odot}	60 R_{\odot}	53 d
Op1.2n6.75e6q50p60	total run	236 R_{\odot}	39 R_{\odot}	29 d

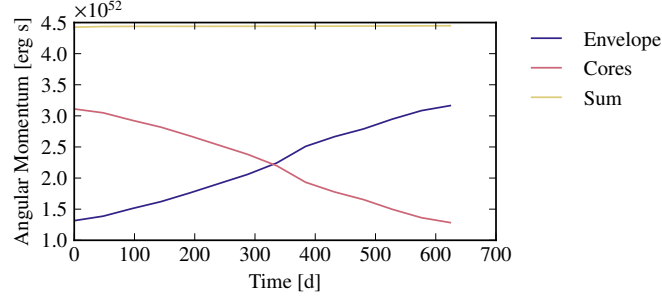


Figure 5.6: Transfer of angular momentum for Op1.2n6.75e6q50p60 until the end of the plunge-in phase.

5.4 Energetic considerations

The transfer of energy from the cores to the envelope (potential and kinetic energy) leads to the unbinding of the mass. In addition, the thermal and internal energy of the envelope itself can be used, especially after the plunge-in when the orbital distance stabilizes. The energetic evolution of the OPAL reference run is shown in Figure 5.7. However, after 2500 d (total error 5.3 %), the error on the energy dominates and we can no longer follow the evolution. We thus chose $t = 2500$ d as end reference for this run.

The unbound mass is defined as the sum of parcels having a positive total energy. It is not clear, how different forms of energy can contribute to the unbinding, we thus distinguish:

- $M_{ej,kin}$, the unbound mass with the kinetic energy exceeding the gravitational binding energy, $e_{pot} + e_{kin} > 0$,
- $M_{ej,therm}$, the unbound mass with the kinetic energy plus thermal energy exceeding the gravitational binding energy, $e_{pot} + e_{kin} + e_{therm} > 0$,
- $M_{ej,int}$, the unbound mass with the kinetic energy plus internal energy (including thermal energy) exceeding the gravitational binding energy, $e_{pot} + e_{kin} + e_{int} > 0$ (OPAL EOS only),

Table 5.3: γ -formalism on the $1.2 M_{\odot}$ primary reference runs. The error can be estimated by $\Delta J_{tot}/J_{tot}^i$, -3.4% (OPAL) resp. 1.6% (ideal gas).

model	$J_{ej}/\text{erg s}$	J_{ej}/J_i	$\Delta M_1/\text{g}$	$\Delta M_1/M_{tot}$	γ
Id1.2n2e6q50p60	1.37×10^{52}	0.28	1.96×10^{32}	0.06	4.5
Op1.2n6.75e6q50p60	6.25×10^{52}	0.42	9.16×10^{32}	0.12	3.5

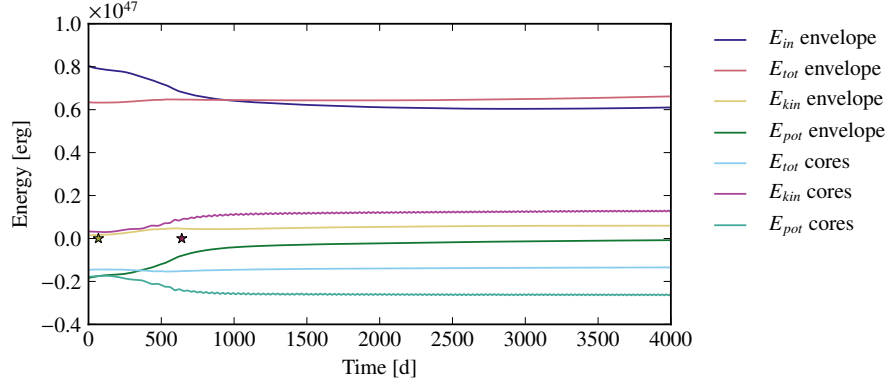


Figure 5.7: Energetic evolution of Op1.2n6.75e6q50p60. The plot shows different energy contributions for cores and envelope separately. The error on the total energy until the end of plunge-in phase it is only 2.0% , however, it is 10.8% ($\Delta E_{tot} = 3.91 \times 10^{45} \text{ erg}$) during the total runtime.

where all energies are expressed as specific energies. For the ideal gas, there is no additional energy contribution to the internal energy from ionization, $e_{int} = e_{therm}$. For clarity in notation and comparison of values, we will refer to it as e_{therm} for the ideal gas EOS, leaving e_{int} undefined. Note that since the cores interact only gravitationally, unlike the gas particles of the envelope, they do not have internal energy.

For the two reference runs, the unbound mass is plotted over time in Figure 5.8. For Id1.2n2e6q50p60, the unbound mass stagnates at about 20% and one can follow the conversion of thermal energy, while in Op1.2n6.75e6q50p60 almost the entire mass is unbound considering the stored internal energy, only the conversion cannot entirely be followed in our simulation. In order to evaluate the outcome, another quantity besides the final orbital separation A_f is the final mass within the orbit of the two cores at the end of the simulation M_{inorb} . If this is low, no further dynamical spiral-in is possible due to the missing transfer of momentum and energy. Since it is about one percent for both runs, we cannot decide whether the cores would merge or find a stable orbit as a close binary system in the further evolution. Table 5.4 lists the unbound mass for different energy contributions at the end of the plunge-in phase. After the plunge-in, about 10% of the envelope's mass are still inside the orbit of the two cores, after the total run, it is about one percent.

The potential and kinetic energies show oscillations due to eccentricity of the orbit.

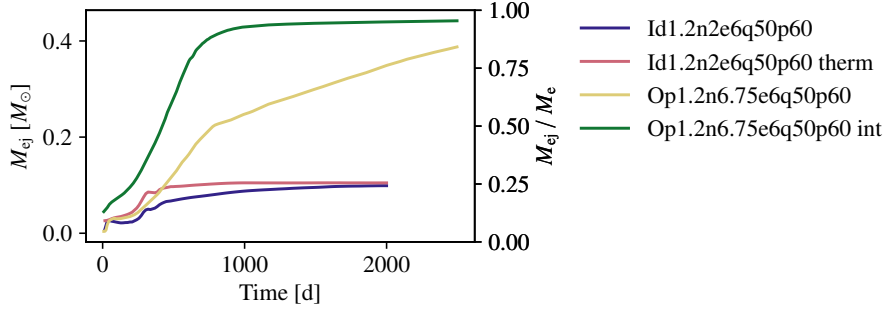


Figure 5.8: By kinetic energy unbound mass (blue resp. yellow line) and by thermal resp. internal energy unbound mass (red resp. green line) over time for Id1.2n2e6q50p60 resp. Op1.2n6.75e6q50p60.

Table 5.4: Different unbound masses of the $1.2 M_{\odot}$ primary reference runs at the end of the plunge-in. The error can be estimated by $\Delta E_{tot}/|E_{pot}^i|$ and is as low as 2.0 % (5.3 %) (OPAL) resp. 0.7 % (1.6 %) (ideal gas) until the end of the plunge-in (the total run).

model	considering	$M_{ej,kin}/M_{tot}$	$M_{ej,therm}/M_{tot}$	$M_{ej,int}/M_{tot}$
Id1.2n2e6q50p60	plunge-in	0.13	0.18	-
Id1.2n2e6q50p60	total run	0.18	0.20	-
Op1.2n6.75e6q50p60	plunge-in	0.40	0.56	0.82
Op1.2n6.75e6q50p60	total run	0.86	0.94	0.98

The total orbital energy, however, does not oscillate. Figure 5.9 shows density slices of the mass still bound considering kinetic energy only. Velocities are highest at the shock fronts, thus, mass becomes unbound there first.

α -formalism

The theoretical value for the envelope structure parameter λ (cf. Section 2.7.2) is not applicable to our model directly since we chose a core criterion with radius and mass much higher than with any physical criterion. The mass product $M_c M_e$ in Equation 2.39 $E_{ce} = -GM_c M_e / \lambda R$ with the constraint $M_e = M_1 - M_c$ is peaked around parity and since for our $1.2 M_{\odot}$ model $M_c \approx M_e$, the mass product is greater than for physical criteria. On the other hand, some of the envelope’s mass is assigned the core, moving the mass-averaged radius of the remaining envelope further outside. With $E_{ee} = -GM_e^2 / 2\lambda R$, for a given value of λ , we would thus overestimate the binding energy of envelope-envelope. For the binding energy of core-envelope, these effects counteract. Due to its extent, the envelope is only tightly bound to itself, giving more weight to the contribution binding of core-envelope. The detailed values are shown in Table 5.5. Combining both and comparing the binding energy $E_{bin,th} = E_{ce} + E_{ee}$ with the actual value from the simulation, we can determine $\lambda \approx 0.26$ for

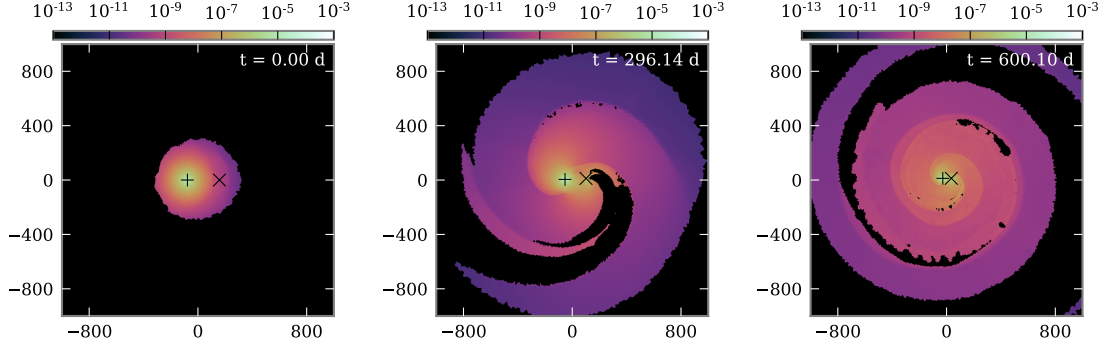


Figure 5.9: Time series of the density of the bound mass considering kinetic energy only (Op1.2n6.75e6q50p60), with color scale ranging from 10^{-13} to $10^{-3} \text{ g cm}^{-3}$. The core of the primary is marked by a +, the secondary by a \times .

Op1.2n6.75e6q50p60 and $\lambda \approx 0.28$ for Id1.2n2e6q50p60. This is in accordance with De Marco et al. [2011] who proposes $\lambda = 0.3$ for a similar AGB star.

Table 5.5: Envelope structure parameter λ for the $1.2 M_{\odot}$ primary. Energies are expressed in terms of 10^{46} erg .

model	E_{ce}	λ_{ce}	E_{ee}	λ_{ee}	E_{bin}	λ
Id1.2n2e6q50p60	-2.7	0.24	-0.7	0.47	-3.4	0.28
Op1.2n6.75e6q50p60	-2.5	0.22	-0.5	0.46	-2.9	0.26

We calculate the values directly from the simulation data. We consider the following quantities:

- binding energy $E_{bin} = E_{pot,tot} - E_{orb}$, the total potential energy except the orbital energy,
- kinetic binding energy $E_{bin,kin} = E_{bin} + E_{kin,env}$, the binding energy including the kinetic energy of the envelope,
- orbital energy $E_{orb} = E_{pot,M2}/2$, sum of potential and kinetic energy leading to factor $1/2$,
- thermal energy E_{therm} , the energy stored in the gas due to temperature,
- internal energy E_{int} , sum of thermal and ionization energy (OPAL only).

The binding energy E_{bin} only serves as sink (plus sign in Δ), the others as sources of energy (minus sign in Δ).

From those quantities, we calculate the following efficiencies:

- $\alpha = -\Delta E_{bin}/\Delta E_{orb}$, the value to compare with the theoretical value,
- $\alpha_{kin} = -\Delta E_{bin,kin}/\Delta E_{orb}$, a more realistic value considering potential and kinetic energies,
- $\alpha_{kin,therm} = -\Delta E_{bin,kin}/\Delta(E_{orb} + E_{therm})$, taking into account the thermal energy as a source,
- $\alpha_{kin,int} = -\Delta E_{bin,kin}/\Delta(E_{orb} + E_{int})$, in case of OPAL EOS, taking into account the entire internal energy.

The minus sign is due to the fact that the quantities in the numerator and denominator are of unequal sign, however, the efficiency $\alpha > 0$.

For the reference runs, the energy differences are listed in Table 5.6, the resulting values for α in Table 5.7. To explain the unbound mass, the thermal contribution is necessary for the ideal gas EOS run (since α and $\alpha_{kin} > 1$ until the end of the plunge-in phase, another energy source is needed). For the OPAL run, the thermal contribution is sufficient until the end of the plunge-in phase, however, in the following internal energy is necessary to explain the unbinding.

Table 5.6: Energies for α -formalism of $1.2 M_{\odot}$ primary reference runs, expressed in terms of 10^{46} erg. The error for the total run (plunge-in) is given by ΔE_{tot} and is 1.9×10^{45} erg (7.1×10^{44} erg) (OPAL) resp. 6.7×10^{44} erg (3.1×10^{44} erg) (ideal gas).

model	considering	ΔE_{bin}	$\Delta E_{bin,kin}$	ΔE_{orb}	ΔE_{therm}	ΔE_{int}
Id1.2n2e6q50p60	plunge-in	1.08	1.34	-0.95	-1.01	-
Id1.2n2e6q50p60	total run	1.44	1.44	-1.49	-1.37	-
Op1.2n6.75e6q50p60	plunge-in	1.10	1.40	-0.69	-0.79	-1.20
Op1.2n6.75e6q50p60	total run	1.75	2.17	-0.90	-1.16	-1.98

Table 5.7: Values of α for $1.2 M_{\odot}$ primary reference runs.

model	considering	α	α_{kin}	$\alpha_{kin,therm}$	$\alpha_{kin,int}$
Id1.2n2e6q50p60	plunge-in	1.13	1.41	0.69	-
Id1.2n2e6q50p60	total run	0.96	0.96	0.50	-
Op1.2n6.75e6q50p60	plunge-in	1.59	2.03	0.95	0.74
Op1.2n6.75e6q50p60	total run	1.93	2.40	1.05	0.75

Here, recombination acts as matter from envelope cools down when spiraling out, further unbinding mass on longer timescales. In our simulations, since no radiation transport is considered, all of the recombination energy released is absorbed by the gas particles. This might not be physical due to low opacities in the outer envelope.

Opacity χ , i.e. the inverse of the mean free path, for the OPAL reference run is shown in Figure 5.10¹. There is a sharp drop at about 10^4 K, i.e. for lower temperatures, in outer regions of lower opacity, i.e. lower optical thickness, the released recombination energy would not be absorbed and used for unbinding, instead, it would get radiated away.

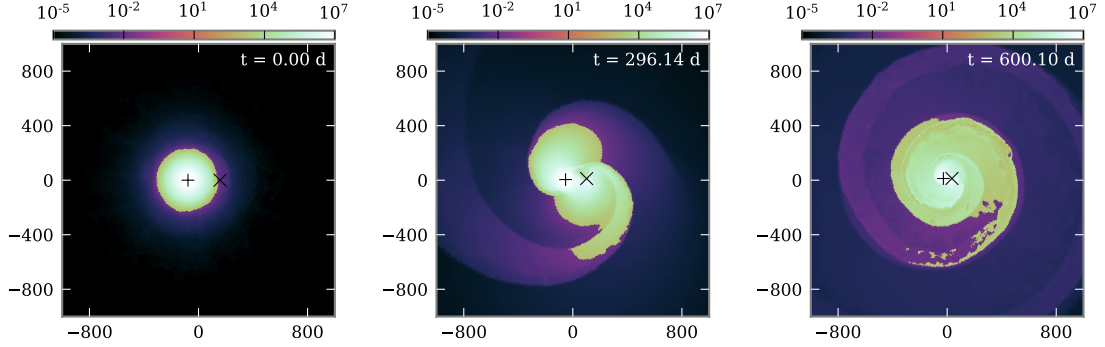


Figure 5.10: Time series of the opacity χ in units of inverse solar radii for Op1.2n6.75e6q50p60, at the beginning of the simulation and after one resp. four orbits in the x - y -plane. The core of the primary is marked by a +, the secondary by a \times .

Our model has a composition of $X = 0.680$ and $Y = 0.300$. Usually, all the helium is recombined before hydrogen recombination starts. Assuming complete ionization at the beginning, a total recombination energy of $\Delta E_{rec} \approx 1.5 \times 10^{46}$ erg is available. This corresponds to a specific recombination energy of $\Delta \epsilon_{rec} \approx 1.8 \times 10^{13}$ erg g⁻¹. Comparing this to the specific gravitational energy,

$$\epsilon_{grav} = -\frac{GM}{r} = -1.9 \times 10^{15} \text{ erg g}^{-1} \left(\frac{M}{M_{\odot}} \right) \left(\frac{R}{R_{\odot}} \right)^{-1}, \quad (5.1)$$

gives a recombination radius of $102 R_{\odot}$ if bound to the total mass of the star and $58 R_{\odot}$ considering only the mass of the giant’s core. These radii are well inside the envelope. Thus, when the gas cools down, recombination takes place and drives the outflow, unbinding the gas. Figure 5.11 shows the released recombination energy for the OPAL reference run. There is a recombination front in the expanding envelope. Regions inside the spiral structure show a lower remaining ionization energy, i.e. energy has been released by recombination, driving the outflow.

¹The opacities outside of the atmosphere depend very much on the temperature on the background grid. In order to depict a meaningful photosphere, the temperature was set to 4×10^3 K in all cells exceeding this temperature where $\rho < 10^{-9}$ g cm⁻³. Mean opacity values are interpolated from tables by the OPAL project [Iglesias and Rogers, 1996] and low-temperature opacities by Ferguson et al. [2005] for $T < 10^4$ K. Since they are dominated by transparent parts of the spectrum, they rather underestimate opacity. Besides, they miss line opacities at the wavelengths of recombination. However, it gives an estimate of the photosphere.

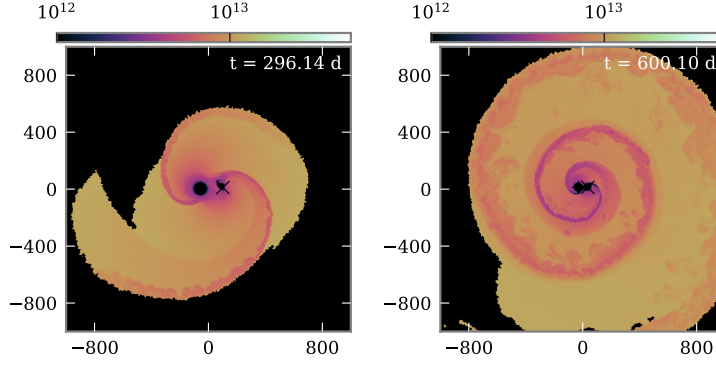


Figure 5.11: Time series of the released specific recombination energy, i.e. the specific ionization energy of a completely ionized gas minus the local specific ionization energy, for Op1.2n6.75e6q50p60, after one resp. four orbits. For better identification, only cells with $\rho > 10^{-10} \text{ g cm}^{-3}$ were considered; the color scale ranges from 10^{12} to $5 \times 10^{13} \text{ erg g}^{-1}$. The core of the primary is marked by a +, the secondary by a x.

5.5 Different companions

The mass of the secondary can take different values within a certain range. More massive companions are unlikely, so we want to focus on ratios smaller unity; we choose $q = 0.25, 0.5, 0.75$.

Table 5.8 shows the orbital values for the plunge-in phase. For OPAL, a more massive companion leads to a faster plunge-in, while there is not a clear tendency for the ideal gas EOS runs. Considering the total run, more massive companions stop their inspiral at greater radii, when there is less than one percent of the envelope's mass left inside the orbit of the two cores. This is accordance with [Passy et al. \[2012\]](#). For "light" companions ($q < 0.34$), they find small final orbital separations and encounter resolution problems. In contrast, we find a great unbound mass fraction when including the recombination energy, which is in accordance with [Sandquist et al. \[1998\]](#), whose observed post-CE binaries must have succeeded in ejecting their envelope. [Schreiber and Gänsicke \[2003\]](#) found no substantial difference during the spiral-in due to phenomena such as magnetic braking or radiation of gravitational waves, as confirmed by [Ohlmann \[2016\]](#).

Table 5.9 compares the unbound mass for different energy contributions with different companions at the end of the plunge-in phase. For the ideal gas EOS, less massive companions can unbind more of the envelope's mass within shorter time, cf. Figure 5.12. More massive companions gravitationally bind ejected mass themselves, the unbound mass fraction thus shows no simple dependence on the mass ratio.

Table 5.10 lists the values for the energy for the total run. Despite the different spiral-in distances, they release about the same orbital energy until all the gas within the orbit of the two cores is expelled. In addition, lighter companions can

Table 5.8: Orbital parameters of the $1.2 M_{\odot}$ primary with different companions (with data from Table 5.2 for completeness) during plunge-in.

model	A_i	P_i	A_f	P_f	$t_{\text{spiral-in}}$
Id1.2n2e6q25p60	205 R_{\odot}	378 d	33 R_{\odot}	24 d	481 d
Id1.2n2e6q50p60	233 R_{\odot}	397 d	52 R_{\odot}	41 d	414 d
Id1.2n2e6q75p60	255 R_{\odot}	406 d	75 R_{\odot}	65 d	462 d
Op1.2n6.75e6q25p60	207 R_{\odot}	385 d	22 R_{\odot}	13 d	670 d
Op1.2n6.75e6q50p60	234 R_{\odot}	409 d	60 R_{\odot}	53 d	572 d
Op1.2n6.75e6q75p60	257 R_{\odot}	418 d	66 R_{\odot}	55 d	559 d

Table 5.9: Unbound mass of the $1.2 M_{\odot}$ primary with different companions at the end of the plunge-in. The error can be estimated by $\Delta E_{\text{tot}}/|E_{\text{pot}}^i|$ and is 2.0 % ($q = 0.5$), 2.9 % ($q = 0.25$) resp. 1.6 % ($q = 0.75$) for OPAL EOS and 0.7 % ($q = 0.5$), 1.4 % ($q = 0.25$) resp. 0.4 % ($q = 0.75$) for ideal gas EOS.

model	$M_{ej,kin}/M_{\odot}$	$M_{ej,therm}/M_{\odot}$	$M_{ej,int}/M_{\odot}$	M_{inorb}/M_{\odot}
Id1.2n2e6q25p60	0.10	0.14	-	0.09
Id1.2n2e6q50p60	0.13	0.18	-	0.10
Id1.2n2e6q75p60	0.03	0.08	-	0.13
Op1.2n6.75e6q25p60	0.22	0.36	0.79	0.15
Op1.2n6.75e6q50p60	0.40	0.56	0.82	0.13
Op1.2n6.75e6q75p60	0.28	0.47	0.78	0.18

use more of the thermal and recombination energy to unbind mass.

The resulting values for α in Table 5.11. To explain the unbound mass, as found above, the thermal contribution is necessary for the ideal gas EOS run. For the OPAL run, the internal energy is necessary to explain the unbinding, while the unbinding is more efficient for more massive companions.

Angular momentum

The values for the γ -formalism are listed in Table 5.12. There is not a clear tendency. The values of γ are generally higher for the OPAL EOS runs, making the unbinding via transfer in angular momentum more efficient.

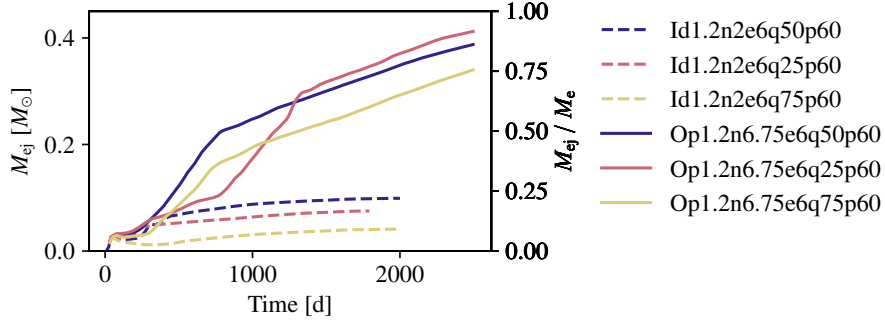


Figure 5.12: By kinetic energy unbound mass over time. Dark blue, red resp. yellow line for $q = 0.5$, $q = 0.25$ resp. $q = 0.75$, dashed line for the ideal gas and continuous line for OPAL EOS.

Table 5.10: Energies for the α -formalism of the $1.2 M_{\odot}$ primary with different companions, expressed in units of 10^{46} erg. The error can be estimated by ΔE_{tot} and is as low as 3.9×10^{45} erg ($q = 0.5$), 2.6×10^{45} erg ($q = 0.25$) resp. 3.38×10^{45} erg ($q = 0.75$) for OPAL EOS and 6.7×10^{44} erg ($q = 0.5$), 9.8×10^{44} erg ($q = 0.25$) resp. 3.0×10^{44} erg ($q = 0.75$) for ideal gas EOS.

model	ΔE_{bin}	$\Delta E_{bin,kin}$	ΔE_{orb}	ΔE_{therm}	ΔE_{int}
Id1.2n2e6q25p60	1.60	1.58	-1.37	-1.40	-
Id1.2n2e6q50p60	1.44	1.44	-1.49	-1.37	-
Id1.2n2e6q75p60	1.42	1.42	-1.33	-1.23	-
Op1.2n6.75e6q25p60	1.87	2.31	-0.95	-1.23	-2.06
Op1.2n6.75e6q50p60	1.86	2.30	-0.92	-1.19	-1.93
Op1.2n6.75e6q75p60	1.84	2.16	-0.75	-1.07	-1.78

Table 5.11: Values of α for $1.2 M_{\odot}$ primary with different companions.

model	α	α_{kin}	$\alpha_{kin,therm}$	$\alpha_{kin,int}$
Id1.2n2e6q25p60	1.17	1.16	0.57	-
Id1.2n2e6q50p60	0.96	0.96	0.50	-
Id1.2n2e6q75p60	1.07	1.07	0.55	-
Op1.2n6.75e6q25p60	1.97	2.43	1.06	0.77
Op1.2n6.75e6q50p60	2.02	2.51	1.09	0.81
Op1.2n6.75e6q75p60	2.45	2.87	1.18	0.85

Table 5.12: γ -formalism on $1.2 M_{\odot}$ primary with different companions. The error can be estimated by $\Delta J_{tot}/J_{tot}^i$ and is as low as -3.4% ($q = 0.5$), 0.9% ($q = 0.25$) resp. -2.4% ($q = 0.75$) for OPAL EOS and 1.6% ($q = 0.5$), 2.5% ($q = 0.25$) resp. 1.3% ($q = 0.75$) for ideal gas EOS (with data from Table 5.2 for completeness).

model	$J_{ej}/\text{erg s}$	J_{ej}/J_i	$\Delta M_1/\text{g}$	$\Delta M_1/M_{tot}$	γ
Id1.2n2e6q25p60	0.96×10^{52}	0.32	1.49×10^{32}	0.06	5.7
Id1.2n2e6q50p60	1.37×10^{52}	0.28	1.96×10^{32}	0.06	4.5
Id1.2n2e6q75p60	0.70×10^{52}	0.10	0.81×10^{32}	0.02	4.7
Op1.2n6.75e6q25p60	2.30×10^{52}	0.84	8.60×10^{32}	0.35	2.4
Op1.2n6.75e6q50p60	6.25×10^{52}	0.42	9.16×10^{32}	0.12	3.5
Op1.2n6.75e6q75p60	4.00×10^{52}	0.67	8.34×10^{32}	0.24	2.7

6 Common envelope simulation with $2.5 M_{\odot}$ primary

In this chapter, we conduct studies with a $2.5 M_{\odot}$ AGB model with radius $99 R_{\odot}$ (for further parameters, see Section 4.8) following Chapter 5. Unlike in the case of the $1.2 M_{\odot}$ model, the total energy of the system is negative, we thus expect the envelope to be only partially unbound afterwards.

Due to the shorter dynamical timescale of 8 d, we expect a faster spiral-in, reducing computational costs. Therefore we choose the initial distance $A_i = 0.8 R_L$ for all of the runs.

The setup is the same as in Chapter 5. For this more massive giant, we choose even smaller ratios of $q = 0.5, 0.25, 0.125$ for the companions. An overview of all setups used in this chapter is shown in Table 6.1.

Table 6.1: Setups for binary runs with $2.5 M_{\odot}$ AGB primary.

Model	EOS	N	q	p
Id2.5n2e6q50p80	ideal gas	2×10^6	1/2	0.8
Op2.5n2e6q50p80	OPAL	2×10^6	1/2	0.8
Op2.5n2e6q25p80	OPAL	2×10^6	1/4	0.8
Op2.5n2e6q125p80	OPAL	2×10^6	1/8	0.8

Unchanged parameters are 5 % cut-off radius and co-rotation $\chi = 95\%$.

The dynamics look similar to the simulations with the $1.2 M_{\odot}$ AGB primary, however, they run on a shorter timescale due to a reduced acoustical timescale of 23 d. The orbital parameters are shown in Table 6.2. At the end of the run, large-scale instabilities, previously described by [Ohlmann \[2016\]](#), emerge from crossing shock layers, cf. Figure 6.1.

Table 6.2: Orbital parameters of the $2.5 M_{\odot}$ primary with different companions.

model	M_2	A_i	A_f	P_f
Id2.5n2e6q50p80	$1.27 M_{\odot}$	$180 R_{\odot}$	$10 R_{\odot}$	2.4 d
Op2.5n2e6q50p80	$1.27 M_{\odot}$	$180 R_{\odot}$	$10 R_{\odot}$	2.5 d
Op2.5n2e6q25p80	$0.64 M_{\odot}$	$158 R_{\odot}$	$5 R_{\odot}$	1.1 d
Op2.5n2e6q125p80	$0.32 M_{\odot}$	$141 R_{\odot}$	$4 R_{\odot}$	0.8 d

The values for the γ -formalism are listed in Table 6.3. Less massive companions yield a greater value of γ , indicating a less effective unbinding by angular momentum.

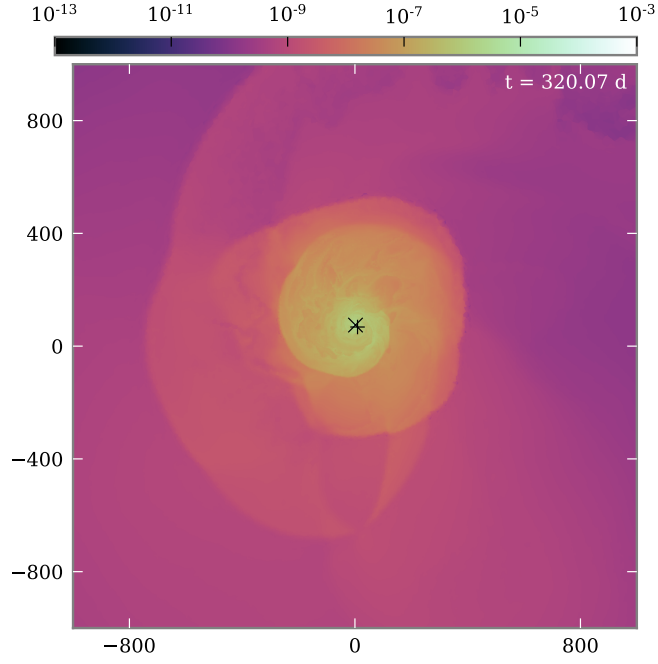


Figure 6.1: Density plot of large-scale instabilities at the end of Op2.5n2e6q50p80. The core of the primary is marked by a +, the secondary by a ×.

Energetic considerations

Table 6.4 compares the unbound masses of the runs. The unbound mass is greater for greater ratios q . The final mass within the orbit of the two cores at the end of the simulation, M_{inorb} , is still significantly higher than in case of the binary simulations with the $1.2 M_{\odot}$ primary, so a further dynamical spiral-in may be possible, but the error on the energy dominates the further evolution.

The values for the envelope structure parameter in this case are $\lambda_{Op} = \lambda_{Id} \approx 0.39$, for both Op2.5n2e6q50p80 and Id2.5n2e6q50p80, cf. Table 6.5. These are higher values compared to the $1.2 M_{\odot}$ model in Chapter 5, as expected for a more massive object [De Marco et al., 2011]. Considering the efficiency of unbinding the envelope by the release of orbital energy, we find that the values for α are smaller than for the binary simulations with the $1.2 M_{\odot}$ primary, however, they show the same tendency.

Table 6.3: γ -formalism on $2.5 M_{\odot}$ primary with different companions. The error can be estimated by $\Delta J_{tot}/J_{tot}^i$ and is as low as 0.9 % ($q = 0.5$), 1.0 % ($q = 0.25$) resp. 1.2 % ($q = 0.125$) (OPAL) resp. 0.7 % (ideal gas).

model	$J_{ej}/\text{erg s}$	J_{ej}/J_i	$\Delta M_1/g$	$\Delta M_1/M_{tot}$	γ
Id2.5n2e6q50p80	4.74×10^{52}	0.32	7.12×10^{32}	0.09	3.4
Op2.5n2e6q50p80	6.25×10^{52}	0.42	9.16×10^{32}	0.12	3.5
Op2.5n2e6q25p80	3.45×10^{52}	0.40	5.97×10^{32}	0.09	4.3
Op2.5n2e6q125p80	1.57×10^{52}	0.30	2.61×10^{32}	0.5	6.4

Table 6.4: Comparison of the energetics of the $2.5 M_{\odot}$ primary with different companions. The error can be estimated by $\Delta E_{tot}/|E_{pot}^i|$ and is as low as 0.3 % ($q = 0.5$) (OPAL and ideal gas), 0.4 % ($q = 0.25$) resp. 0.2 % ($q = 0.125$).

model	$M_{ej,kin}/M_{\odot}$	$M_{ej,therm}/M_{\odot}$	$M_{ej,int}/M_{\odot}$	M_{inorb}/M_{\odot}
Id2.5n2e6q50p80	13 %	15 %	-	9.8 %
Op2.5n2e6q50p80	15 %	19 %	28 %	13.1 %
Op2.5n2e6q25p80	11 %	13 %	16 %	6.7 %
Op2.5n2e6q125p80	5 %	5 %	7 %	32.7 %

Table 6.5: Envelope structure parameter λ for the reference runs. Energies are expressed in terms of 10^{47} erg.

model	E_{ce}	λ_{ce}	E_{ee}	λ_{ee}	E_{bin}	λ
Op2.5n2e6q50p80	-1.4	0.29	-1.7	0.47	-3.1	0.39
Id2.5n2e6q50p80	-1.4	0.29	-1.6	0.48	-3.1	0.39

Table 6.6: Values of α for $2.5 M_{\odot}$ primary with different companions.

model	α	α_{kin}	$\alpha_{kin,therm}$	$\alpha_{kin,int}$
Id2.5n2e6q50p80	0.68	0.79	0.45	-
Op2.5n2e6q50p80	1.17	1.36	0.65	0.70
Op2.5n2e6q25p80	1.34	1.58	0.71	0.76
Op2.5n2e6q125p80	1.43	1.58	0.69	0.73

7 Conclusion

The angular momentum of the cores as well as their potential energy are continuously transferred to the envelope during the plunge-in phase. A stream onto the companion accretes mass on it and creates a shock, forming spiral arms. Due to the shock moving through the atmosphere, on the opposite side of the envelope, another arm forms. With this spiral structure, matter gets transported outwards and ejected.

The transfer of potential energy of the cores to the envelope mainly acts in close vicinity of the cores and within the softening length of the gravitational interaction of the point masses. We thus require a high resolution of the softening length in order to minimize the energy error.

Like [Ohlmann \[2016\]](#), we observe shear instabilities between single layers of the spiral structure of the ejected mass due to the spiral-in of the companion. When these instabilities mix in case of the binary simulations performed with the $2.5 M_{\odot}$ primary, large-scale flow instabilities arise; the thereby caused turbulent convection changes energy transport. For the less massive and more extended $1.2 M_{\odot}$ primary, no large-scale flow instabilities are observed, the spiral structure is preserved.

Including recombination leads to similar dynamics, however, the ejected mass is increased. Recombination acts behind spiraling shocks where the gas cools, boosting the expansion. Since due to the energy error we cannot follow the recombination until the stagnation of the unbound mass fraction in our simulations, we can assess this quantity including the recombination energy still stored in the gas in the energetic consideration. This may overestimate the unbound mass fraction, since not all of it can be converted, but with this consideration, the envelope may be ejected completely in our simulations. Regarding the opacities of the envelope, we can identify the photosphere of the AGB star. From there, a recombination shock front spirals out, driving the outflow.

The evolution of the orbital separation including recombination is very similar to the ideal gas EOS simulation. Less massive companions spiral in deeper, while mass is unbound with about the same efficiency α . For $q \lesssim 0.5$, the unbound mass fraction increases. For more massive companions, ejected gas remains bound to the binary system. The γ -formalism for the efficiency of unbinding the envelope by angular momentum does not yield a clear result in our simulations. For the $1.2 M_{\odot}$ primary, the spiral-in stops when all mass is outside the orbit of the two cores. The third phase, the self-regulating spiral-in, is missing further envelope material to interact with. For the $2.5 M_{\odot}$ primary, the energy error accumulated during this slow spiral-in becomes too big. Thus, no statement about the outcome, whether the cores would merge or remain as a close binary system, can be made.

Outlook

An implementation of multi-wavelength radiative transport in the envelope is necessary in order to further investigate of the processes involved in unbinding.

A better resolution of the softening length of the gravitational interaction of the point masses might not be necessary for a stable AGB model, however, it may further reduce the energy error during the run, allowing for a longer runtime. Resolving more of the envelope's mass by reducing the cut-off radius may then allow to follow the spiral-in longer and determine the outcome.

Nomenclature

Acronyms

AGB	asymptotic giant-branch
CE(E)	common(-)envelope (evolution)
EOS	equation of state
MS	main sequence
WD	white dwarf

Greek Symbols

α_{CE}	efficiency of energy conversion in CEE, $\alpha_{CE} = \frac{E_{bin}}{\Delta E_{orb}}$
γ	inverse of unbinding efficiency by angular momentum

Roman Symbols

A	orbital separation
P	orbital period
p	relative initial separation, $p = \frac{A_i}{R_L}$
q	mass ratio, $q = \frac{M_2}{M_1}$
R_L	Roche lobe radius
r_{cut}	relative cut-off radius of the point mass replacing the giant's core

Subscripts

$1/2$	primary (AGB)/secondary (WD) parameter
c/e	primary (AGB) core/envelope parameter
ej	ejected
i/f	initial/final value
$inorb$	within the orbit of the two cores

Part I

Appendix

A Constants

We use the centimetre–gram–second system of units (CGS or cgs).

Table A.1: Overview CGS units.

Quantity	Symbol	CGS unit	definition	in SI units
length, position	L, x	centimeter (cm)	m/100	= 10-2 m
mass	m	gram (g)	kg/1000	= 10-3 kg
time	t	second (s)	second	= 1 s
velocity	v	cm/s	cm s-1	= 10-2 m s-1
acceleration	a	gal (Gal)	cm s-2	= 10-2 m s-2
force	F	dyne (dyn)	g cm s-2	= 10-5 N
energy	E	erg (erg)	g cm2 s-2	= 10-7 J
power	P	erg/s	g cm2 s-3	= 10-7 W
pressure	p	barye (Ba)	g cm-1 s-2)	= 10-1 Pa
dynamic viscosity	μ	poise (P)	g cm-1 s-1	= 10-1 Pa s
kinematic viscosity	ν	stokes (St)	cm2 s-1	= 10-4 m2 s-1
wavenumber	k	kayser (K)	cm-1	= 100 m-1
momentum	p		g cm s-1	= 10-5 kg m s-1
angular momentum	L		g cm2 s-1 = erg s	= 10-7 kg m2 s-1 = 10-7 J s

Table A.2: List of constants used.

Quantity	symbol	value
gravitational constant	G	$6.672\,59(85) \times 10^{-8} \text{ cm}^3 \text{ g}^{-1} \text{ s}^{-2}$
solar mass	M_{\odot}	$1.99 \times 10^{33} \text{ g}$
solar radius	R_{\odot}	$6.96 \times 10^{10} \text{ cm}$
solar luminosity	L_{\odot}	$3.9 \times 10^{33} \text{ erg s}^{-1}$
solar temperature	T_{\odot}	$5.780 \times 10^3 \text{ K}$

B List of Figures and Tables

B.1 List of Figures

2.1	Ellipse with annotations.	11
2.2	3D Roche potential.	12
3.1	Voronoi tessellation.	19
4.1	Hertzsprung-Russell diagram of $1.2 M_{\odot}$ model.	22
4.2	Profiles of different quantities of the initial conditions.	24
4.3	Comparison for softening length resolution 20 and 40.	25
4.4	Density profile of relaxation.	26
4.5	Comparison of ideal gas and OPAL EOS.	27
4.6	Mach plots of $1.2 M_{\odot}$ OPAL relaxation simulation.	28
5.1	Orbital evolution.	32
5.2	Time series of density plots.	33
5.3	Mach numbers in orbital plane.	33
5.4	Mach numbers in perpendicular plane.	34
5.5	Comparison of orbital distance evolution.	34
5.6	Transfer of angular momentum.	35
5.7	Energetic evolution.	36
5.8	Unbound mass evolution.	37
5.9	Bound mass considering kinetic energy.	38
5.10	Opacity evolution.	40
5.11	Released specific recombination energy evolution.	41
5.12	Unbound mass evolution with different companions.	43
6.1	Large-scale instabilities.	46

B.2 List of Tables

4.1	Parameters of MESA profiles	22
4.2	Energy conservation $1.2 M_{\odot}$ model, different resolutions.	27
4.3	Deviations of the energy during the relaxation.	28
4.4	Final AGB model parameters.	29
5.1	Setups for binary runs with $1.2 M_{\odot}$ AGB.	31
5.2	Orbital parameters of the reference runs with $1.2 M_{\odot}$ primary.	35

5.3	γ -formalism on $1.2 M_{\odot}$ primary reference runs.	36
5.4	Different unbound masses of the $1.2 M_{\odot}$ primary reference runs. . . .	37
5.5	λ parameter for $1.2 M_{\odot}$ primary.	38
5.6	Energies for the α -formalism.	39
5.7	Values of α for $1.2 M_{\odot}$ primary reference runs.	39
5.8	Orbital parameters during plunge-in with different companions. . . .	42
5.9	Unbound mass with different companions.	42
5.10	Energies for α -formalism of $1.2 M_{\odot}$ primary with different companions.	43
5.11	Values of α for $1.2 M_{\odot}$ primary with different companions.	43
5.12	γ -formalism with different companions.	44
6.1	Setups for binary runs with $2.5 M_{\odot}$ AGB.	45
6.2	Orbital parameters of the $2.5 M_{\odot}$ primary with different companions.	45
6.3	γ -formalism on $2.5 M_{\odot}$ primary with different companions.	47
6.4	Energetics of the $2.5 M_{\odot}$ primary with different companions.	47
6.5	λ parameter for $2.5 M_{\odot}$ primary reference runs	47
6.6	Values of α for $2.5 M_{\odot}$ primary with different companions.	47
A.1	CGS units.	52
A.2	Constants	52

C Bibliography

- Matthew Benacquista. *An Introduction to the Evolution of Single and Binary Stars*. Springer New York, New York, 2013.
- Bradley W Carroll and Dale A Ostlie. *An introduction to modern astrophysics*. Cambridge University Press, 2017.
- M. de Kool. Common envelope evolution and double cores of planetary nebulae. *The Astrophysical Journal*, 358:189–195, July 1990. doi: 10.1086/168974.
- O. De Marco, E. L. Sandquist, M.-M. Mac Low, F. Herwig, and R. E. Taam. Wolf-Rayet Central Stars and the Binary Evolution Channel. In M. Reyes-Ruiz and E. Vázquez-Semadeni, editors, *Revista Mexicana de Astronomía y Astrofísica Conference Series*, volume 18, pages 24–30, September 2003.
- Orsola De Marco, Jean-Claude Passy, Maxwell Moe, Falk Herwig, Mordecai-Mark Mac Low, and Bill Paxton. On the α -formalism for the common envelope interaction. 2011.
- Peter Eggleton. *Evolutionary Processes in Binary and Multiple Stars*. Cambridge University Press, Cambridge, New York, 2006.
- Peter P. Eggleton. Approximations to the radii of Roche lobes. *The Astrophysical Journal*, 268:368, May 1983. doi: 10.1086/160960.
- J. W. Ferguson, D. R. Alexander, F. Allard, T. Barman, J. G. Bodnarik, P. H. Hauschildt, A. Heffner-Wong, and A. Tamanai. Low-Temperature Opacities. *The Astrophysical Journal*, 623:585–596, April 2005. doi: 10.1086/428642.
- H. Glanz and H. B. Perets. Efficient common-envelope ejection through dust-driven winds. *ArXiv e-prints*, January 2018.
- K. M. Górski, E. Hivon, A. J. Banday, B. D. Wandelt, F. K. Hansen, M. Reinecke, and M. Bartelmann. HEALPix: A Framework for High-Resolution Discretization and Fast Analysis of Data Distributed on the Sphere. *The Astrophysical Journal*, 622:759–771, April 2005. doi: 10.1086/427976.
- C. A. Iglesias and F. J. Rogers. Updated Opal Opacities. *The Astrophysical Journal*, 464:943, June 1996. doi: 10.1086/177381.
- N. Ivanova and J. L. A. Nandez. Common envelope events with low-mass giants: understanding the transition to the slow spiral-in. *Monthly Notices of the Royal Astronomical Society*, 462:362–381, October 2016. doi: 10.1093/mnras/stw1676.

- N. Ivanova, S. Justham, X. Chen, O. De Marco, C. L. Fryer, E. Gaburov, H. Ge, E. Glebbeek, Z. Han, X.-D. Li, G. Lu, T. Marsh, P. Podsiadlowski, A. Potter, N. Soker, R. Taam, T. M. Tauris, E. P. J. van den Heuvel, and R. F. Webbink. Common envelope evolution: where we stand and how we can move forward. *The Astronomy and Astrophysics Review*, 21:59, February 2013. doi: 10.1007/s00159-013-0059-2.
- R. G. Izzard, P. D. Hall, T. M. Tauris, and C. A. Tout. Common envelope evolution. In *IAU Symposium*, volume 283 of *IAU Symposium*, pages 95–102, August 2012. doi: 10.1017/S1743921312010769.
- R. Kippenhahn and A. Weigert. *Stellar Structure and Evolution*. Springer-Verlag, Berlin, Heidelberg, 1990.
- G. Nelemans, F. Verbunt, L. R. Yungelson, and S. F. Portegies Zwart. Reconstructing the evolution of double helium white dwarfs: envelope loss without spiral-in. *Astronomy and Astrophysics*, 360:1011–1018, August 2000.
- Sebastian T. Ohlmann. *Hydrodynamics of the Common Envelope Phase in Binary Stellar Evolution*. PhD thesis, Ruperto-Carola University of Heidelberg, 2016.
- B. Paczynski. Common Envelope Binaries. In P. Eggleton, S. Mitton, and J. Whelan, editors, *Structure and Evolution of Close Binary Systems; Proceedings of the Symposium, Cambridge, England, July 28-August 1, 1975*, volume 73 of *IAU Symposium*, page 75, 1976.
- B. Paczyński and J. Ziółkowski. Evolution of Close Binaries. III. *Acta Astronomica*, 17:7, 1967.
- J.-C. Passy, O. De Marco, C. L. Fryer, F. Herwig, S. Diehl, J. S. Oishi, M.-M. Mac Low, G. L. Bryan, and G. Rockefeller. Simulating the Common Envelope Phase of a Red Giant Using Smoothed-particle Hydrodynamics and Uniform-grid Codes. *The Astrophysical Journal*, 744:52, January 2012. doi: 10.1088/0004-637X/744/1/52.
- Bill Paxton, Lars Bildsten, Aaron Dotter, Falk Herwig, Pierre Lesaffre, and Frank Timmes. Modules for experiments in stellar astrophysics (mesa). *The Astrophysical Journal Supplement Series*, 192(1):3, 2010.
- Philipp Podsiadlowski. The evolution of binary systems. pages 45–88, 01 2012.
- Frederic A. Rasio and Mario Livio. On the formation and evolution of common envelope systems. *The Astrophysical Journal*, 471(1):366, 1996. URL <http://stacks.iop.org/0004-637X/471/i=1/a=366>.
- F. J. Rogers and A. Nayfonov. Updated and Expanded OPAL Equation-of-State Tables: Implications for Helioseismology. *The Astrophysical Journal*, 576:1064–1074, September 2002. doi: 10.1086/341894.

- E. L. Sandquist, R. E. Taam, X. Chen, P. Bodenheimer, and A. Burkert. Double Core Evolution. X. Through the Envelope Ejection Phase. *The Astrophysical Journal*, 500:909–922, June 1998. doi: 10.1086/305778.
- M. R. Schreiber and B. T. Gänsicke. The age, life expectancy, and space density of Post Common Envelope Binaries. *Astronomy and Astrophysics*, 406:305–321, July 2003. doi: 10.1051/0004-6361:20030801.
- Marcel Vincent van der Sluys. *Formation and evolution of compact binaries*. PhD thesis, Utrecht University, 2006.
- N. Soker. Energizing the last phase of common-envelope removal. *Monthly Notices of the Royal Astronomical Society*, 471:4839–4843, November 2017. doi: 10.1093/mnras/stx1978.
- Volker Springel. E pur si muove: Galilean-invariant cosmological hydrodynamical simulations on a moving mesh. 2010.
- R.F. Webbink. Common Envelope Evolution Redux. In *Short-Period Binary Stars: Observations, Analyses, and Results. Astrophysics and Space Science Library, vol 352*. Springer, Dordrecht, 2008.